ABSTRACT

Title of Document: NANOSTRUCTURED NICKEL-ZINC MICROBATTERIES USING THE TOBACCO MOSAIC VIRUS

Konstantinos Gerasopoulos, Master of Science, 2008

Directed By: Professor Reza Ghodssi, Department of Electrical and Computer Engineering

The development of nanostructured nickel electrodes using the *Tobacco mosaic virus* (TMV) for microbattery applications is presented in this Thesis. The TMV is a high aspect ratio cylindrical plant virus that can be used as a template to increase reactive surface area in MEMS-fabricated batteries. Genetically modifying the virus to display multiple binding sites allows for nickel metallization and self-assembly onto various substrates. In this work, the TMV biofabrication technique has been integrated into standard MEMS fabrication processes and novel nickel-zinc microbatteries have been developed using this technology. The nanostructured batteries exhibited appropriate charge-discharge response for up to thirty cycles of operation and demonstrated a six-fold increase in capacity compared to devices with planar electrode geometries. These results, combined with the simplicity and compatibility of the TMV assembly with various MEMS processes, make this approach promising for the development of compact, high-performance small-scale energy conversion devices.

NANOSTRUCTURED NICKEL-ZINC MICROBATTERIES USING THE TOBACCO MOSAIC VIRUS

By

Konstantinos Dimitriou Gerasopoulos

Thesis submitted to the Faculty of the Graduate School of the
University of Maryland, College Park, in partial fulfillment
of the requirements for the degree of
Master of Science
2008

Advisory Committee:
Professor Reza Ghodssi, Chair
Professor Martin Peckerar
Professor James Culver

Dedication

To my parents, Dimitri and Eleni, my brother, Vasili, and Irene, for their continuous love and support. Also, Professor Maria Klapa for trusting in my abilities.

Acknowledgements

I would like to acknowledge the help and contribution of my advisor, Professor Reza Ghodssi, for his guidance and support throughout the course of this work, and the rest of my Thesis Committee members, Professor Martin Peckerar and Professor James Culver. Also, the Laboratory for Physical Sciences (LPS) for funding this project, my colleagues in this work, Dr. Matthew McCarthy for his invaluable assistance during this project, and Dr. Elizabeth Royston, for introducing me to the world of the *Tobacco mosaic virus*, Mr. Ayan Ghosh and Professor Peter Kofinas for providing access to a state-of-the-art potentiostat and assisting me with the data acquisition.

I would like to thank all the people who provided assistance in the fabrication at the LPS and Mayrland Nanocenter clean-room facilities: Mr. Michael Khbeis, Mr. Toby Olver, Mr. George DeLa Vergne, Mrs. Lisa Lucas, Mr. Tom Loughran and Mr. Jon Abrahams. Also, my colleague Mr. Nathan Siwak, Dr. Wen-Ahn Chou and Mr. Larry Lei for taking SEM images and the people at the Physics Machine Shop for the macro-scale machining in this work.

Last, but not least, all my colleagues at the MEMS Sensors & Actuators Lab for insightful discussions and suggestions during presentations. I would particularly like to acknowledge the PowerMEMS group, Dr. Nima Ghalichechian, Dr. Christopher M. Waits, Mr. Mustafa Ilker Beyaz, Mr. Brendan Hanrahan and Mr. Lance Mosher, for numerous hours of discussions and paper revisions. Finally, my roommates, Mr. Michael Hughes, Mr. Alexander Tzannes, Mr. Owen McDonough and Mr. Arthrur Winter.

Table of Contents

Dedication ii
Acknowledgements iii
Table of Contents v
List of Tables viii
List of Figures x
Chapter 1: Introduction 1
1.1 Motivation and Objective 2
1.2 Device Overview 5
1.3 Review of Related Work 6
1.3.1 MEMS Fabricated Batteries 6
1.3.2 Nanostructured Batteries and Electrodes 10
1.3.3 Microgenerators and Fuel Cells 11
1.3.4 Electroless Plating 14
1.3.5 Fabrication and Bonding with SU-8 16
1.4 Thesis Contributions and Outline 19
Chapter 2: Fundamental Concepts of Electrochemistry 21
2.1 Electrochemical Cell 21
2.2 Performance Parameters 23
2.2.1 Battery Voltage 23
2.2.2 Battery Capacity 24
2.3 Classification of Batteries 26
2.4 Analysis and Design 27
2.4.1 Battery Model 27
2.4.2 Voltage Levels 29
2.4.3 Effect of temperature 30
Chapter 3: The *Tobacco mosaic virus* as a Nanoscale Template 32
3.1 Structure 33
3.2 Engineered Mutations 35
3.3 Metallization and Applications 37
Chapter 4: Design and Fabrication 41
4.1 Design 41
4.1.1 Chemistry 41
4.1.2 Device 42
4.2 Fabrication 44
4.2.1 Process Flow 44
4.2.2 Structural SU-8 45
4.2.3 TMV Self-assembly and Metallization 51
4.2.4 Adhesive Bonding with SU-8 55
Chapter 5: Testing and Results 59
5.1 Testing Apparatus 59
5.1.1. Microfluidic Package 59
5.1.2 Potentiostat Operation 61
5.2 Initial Results 63

5.3 Characterization 65
5.3.1 Charge – Discharge Response 66
5.3.2 Effect of TMV Coating 67
5.3.3 Device Repeatability 68
5.3.4 Effect of Electrode Gap 70
5.4 Summary 71
Chapter 6: Future Work and Conclusions 73
6.1 Continued Work 73
6.1.1 Limitations 73
6.1.2 Nano- and micro-fabrication development using the TMV 75
6.1.3 Future Designs 77
6.2 Thesis Conclusions 79
Appendix A - Solution Preparation 80
Appendix B – AutoCAD files 81
References 83

List of Tables

Table 1.1 – Summary of MEMS fabricated batteries …….....9

Table 4.1 – Process parameters for structural SU-8 layer……. 50

Table 5-1 – Potentiostat parameters ……..63

List of Figures

Figure 1.1: Conceptual schematic showing a smart dust mote and its basic components [2].....3

Figure 1.2: Three-dimensional view of the microbattery device…….…….....5

Figure 1.3: SEM images of (a) the disposable battery presented in [5], (b) the nickel-zinc battery of [6],with the nickel electrode on the left and the zinc electrode on the right, (c) the water-activated battery of[8] and (d) the solid-electrolyte battery layer arrangement of [11].…….....7

Figure 1.4: Schematic representation of the lithium-based batteries presented in [13] and [25] respectively (a-b) and SEM images of the microposts of [14] for nickel-zinc and lithium-ion batteries (c-d) ……8

Figure 1.5: (a) SEM image of as-prepared ZnO nanorods [20] and (b) schematic representation of a flexible energy storage device [22] ……10

Figure 1.6: (a) SEM image of a nickel coated TMV electrode [24] and (b) TEM images of a cobalt oxide M-13 viral nanowires [23] ……11

Figure 1.7: (a) Schematic of the electromagnetic generator described in [26], (b) image of the thermoelectric generator structure of [29] and (c) cross-sectional view of a cantilever for piezoelectric energy harvesting [30]……..13

Figure 1.8: (a) SEM image of a high surface area carbon electrode for a bio-synthetic fuel cell [35], (b) high surface area microfabricated structures for a solid-oxide fuel cell [34], (c) schematic representation of fuel reformer [36] and optical image of a fuel cell microreactor [37].…….....13

Figure 1.9: Magnetic structures fabricated using electroless plating of rare-earth metals [45]……..15

Figure 1.10: SEM image of a six-layer SU-8 microstructure fabricated using the process described in [48]. Each layer is numbered in the order it was patterned……16

Figure 1.11: Use of SU-8 for electroplating with a photoresist sacrificial layer: (a) the sacrificial layer is patterned, (b) seed layers are deposited, (c) the SU-8 mold is created and (d) the free-standing structure is released [51].……17

Figure 1.12: (a) Polymer micromirrors fabricated in SU-8 [14] and (b) a microfluidic system made in SU-8 containing waveguides, a laser resonator and microfluidic channels [11]……18

Figure 1.13: Schematic representation of the fabrication process described in [59] for the fabrication of multi-layer fluidic networks in SU-8.……..……19

Figure 2.1: (a) Discharge mode of operation (b) charge mode of operation…....….22

Figure 2.2: Cell polarization as a function of operating current [61]……..28

Figure 2.3: Cell polarization as a function of operating current [61]……..30

Figure 2.4: Typical voltage profile on charge and discharge [61]…….……..30

Figure 2.5: Effect of temperature in battery capacity [61]…….……..31

Figure 3.1: (a) TEM image of wild-type viruses, (b) simplified model of the TMV structure [63]……34

Figure 3.2: Model of the TMV disk showing the various amino acids [67]……..….35

Figure 3.3: Structural location of the TMV1cys mutation: (a) Top view showing half of a coat protein layer within the TMV rod and (b) 2X magnification of an edge view for the same coat protein layer (location of the 1cys mutations are highlighted in yellow)……..…..……..37

Figure 3.4: Concept and operation of the TMV-based digital memory device of [74]…….....38

Figure 3.5: Demonstration of the patterned TMV assembly on a chitosan-mediated electrode using DNA hybridization [73]……...……...….....39

Figure 3.6: TEM image showing a 70 nm thick cross-section of nickel-coated TMV1cys attached perpendicular to a gold surface. Scale bar is equal to 300 nm [24]…….....40

Figure 4.1: Three-dimensional view of the microbattery layers…...……...43

Figure 4.2: Fabrication process flow: (a) LPCVD of a SiO2 film, (b) E-beam evaporation of Cr/Au, (c)structural SU-8 lithography, (d) TMV self-assembly and coating process, (e) patterning of the bonding SU-8 layer, and (f) bonding with the zinc anode……44

Figure 4.3: Image of the transparency mask used for the structural SU-8 fabrication……46

Figure 4.4: (a) Crack formation for underexposed structures and (b) resolved problem after exposure……...47

Figure 4.5: SU-8 structures using (a) SU-8 2002 as adhesion promoter and (b) reduced baking temperatures……...49

Figure 4.6: Schematic representation of the TMV assembly and nickel coating process: the TMV binds on the gold surface (step 1), activated with a palladium catalyst (step 2) and finally coated with nickel (step 3)…….....51

Figure 4.7: SEM images at two magnifications of nickel electrodes with (a,b) and without (c,d) TMV coatings…….....54

Figure 4.8: SEM image of nickel electrodes at TMV concentrations of 0.05 mg/mL (left) and 0.01 mg/mL(right)……...54

Figure 4.9: SEM images of (a) a zinc piece bonded with the patterned SU-8 layer, (b) TMV structures on the structural SU-8 layer covered in SU-8 and (c) a bonded test structure of two silicon chips used in estimating the bond thickness…….....56

Figure 4.10: Image of a microbattery diced in half and its cross-sectional schematic….....58

Figure 5.1: Image of a packaged microbattery showing the fluidic and electrical connections…….....60

Figure 5.2: Image of the potentiostat software interface……....62

Figure 5.3: Charge-discharge curve of a TMV microbattery under the initial testing conditions…….……64

Figure 5.4: Charge-discharge curve of a TMV microbattery under modified operating conditions for the first 8 cycles of operation……...…66

Figure 5.5: Capacity versus cycle number for a TMV modified device with 0.64 cm^2 footprint area and electrode spacing of 65 μm…….. 67

Figure 5.6: Initial discharges of cells with and without TMV coatings……..68

Figure 5.7: Capacity versus cycle number for three TMV modified devices with 0.64 cm^2 footprint area and electrode spacing of 65 μm.……... 69

Figure 5.8: Voltage versus time graph for one discharge cycle of devices with different electrode gaps……..……. 70

Figure 5.9: Capacity versus cycle number for devices with different electrode spacings……71

Figure 6.1: Schematic representation of a likely mechanism for device failure – dendrite formation from the zinc anode to the conductive SU-8 sidewalls…….74

Figure 6.2: SEM image of gold-covered silicon chip with nickel-coated TMV nanostructures that have been patterned using lift-off…….....76

Figure 6.3: Schematic representation of a future microbattery design (the yellow and green structures correspond to two different battery electrode materials)……...77

Chapter 1: Introduction

MicroElectroMechanical Systems (MEMS) is a relatively new engineering field that is aiming towards the miniaturization of sensors, actuators and systems, following a trend similar to the one that sparked the electronic industry revolution after the 1950s. The term MEMS is used to describe the integration of sensing and actuating mechanisms with electronic components on the same chip for the realization of small, compact and intelligent systems. While the acronym in the early days was used to refer to devices with electrical and movable components, continuous research has led to the development of various new applications that span from life sciences and bioengineering (BioMEMS and micro-total analysis systems) to small-scale power generation and energy conversion (PowerMEMS). The advantage of MEMS technology lies in the scaling properties of the different transduction mechanisms (e.g. electrical, magnetic, thermal etc) and structural materials [1] that allow MEMS devices to be faster, more energy-efficient and more sensitive than their macroscopic counterparts.

MEMS fabrication was initially based on techniques used in or compatible with the IC industry such as photolithography, thin-film deposition and patterning and surface micromachining, the successive deposition and patterning of structural and sacrificial layers. Over the years however, the breadth of emerging applications and enabling technologies have resulted in the development of several new processes, ranging from basic bulk micromachining (the fabrication of device structures by selective removal of areas in the silicon substrate using wet or dry chemical processes) to three-dimensional photolithography and patterning (gray-scale,

electroplating), as well as the use of alternative metals and dielectrics and novel polymer materials (PDMS, SU-8). Using MEMS technology, several devices including pressure and inertial sensors and micro-mirrors for projection displays have been commercialized, demonstrating the advantages offered by miniaturization and batch fabrication at low cost. Ongoing research both at the academic and industrial level is expected to increase the number of commercial applications and therefore significantly impact every-day life.

1.1 Motivation and Objective

A major challenge towards the realization of autonomous integrated microsystems is power generation and energy storage. While MEMS sensors and actuators can be designed and fabricated with improved performance compared to macroscopic devices, bulky external equipment is required for their proper operation and remains the key limiting factor for their use in applications outside the laboratory environment, such as homeland security, building and equipment monitoring and space navigation. These applications envision systems with various sensing mechanisms (temperature, pressure, shear stress, humidity, poisonous gases and liquids) and the appropriate low-power electronic components for operation and wireless data communication. In many cases, it is desirable that a scavenging mechanism will be integrated with the system to harvest energy from available sources adjacent to the device and therefore recharge the power generating components after several communication cycles have been completed.

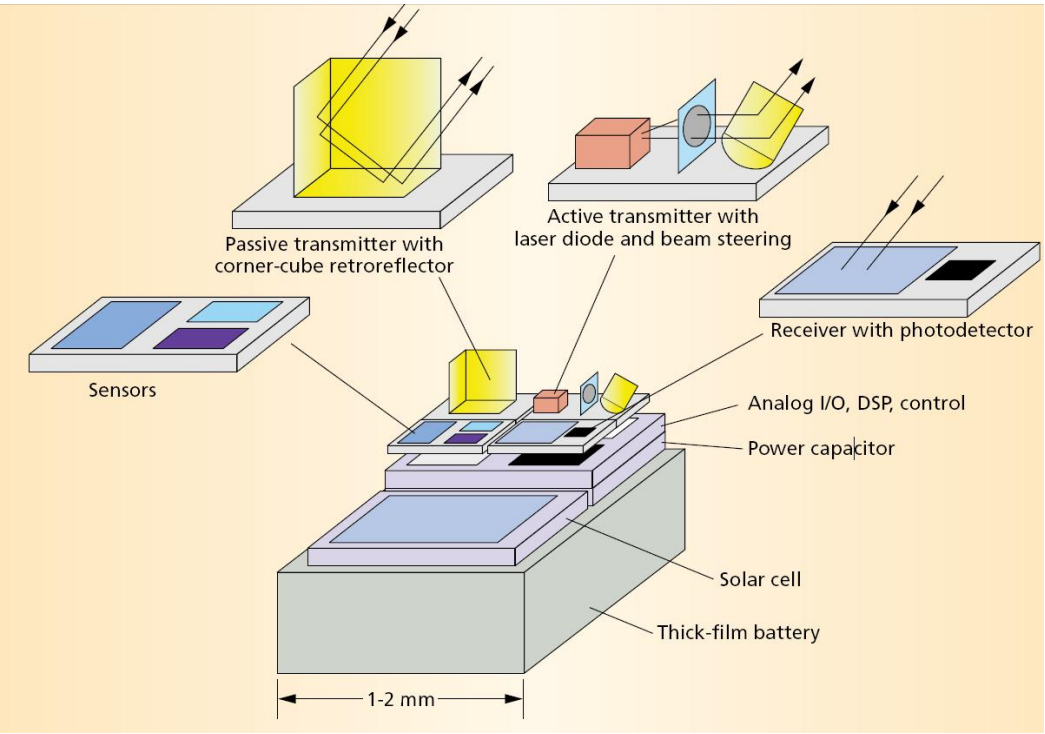

Figure 1.1: Conceptual schematic showing a smart dust mote and its basic components [2].

An example of such wireless distributed sensor nodes, often coined with the term "smart-dust motes" in the open literature, is shown in Figure 1.1 [2]. This particular mote consists of sensors, wireless transmitters and receivers, a solar cell array that harvests energy from ambient light and stores it in a super capacitor to ensure continuous operation during periods of darkness, and a thick-film battery to power the various electrical components. Through the use of MEMS microfabrication technologies and packaging, these nodes are designed to be in the order of a few to ten cubic millimeters, which will allow mass-production and deployment in multiple sites. As these systems are scaled down however, available surface area limits the performance of the required microbatteries, since electrochemical conversion is a surface area-dependent phenomenon.

The need for power generation and energy storage devices that will fulfill the energy requirements of such wireless systems is of particular importance. Several studies have been conducted to investigate and quantify the power requirements of these applications [3, 4]. While the power needed for operation of the sensors is in the order of a few tens of microwatts, this requirement is increased by up to three orders of magnitude for the short periods of transmission and communication and a traditional thin-film battery would have to occupy a large surface area to ensure proper operation under these conditions. Therefore, development of microbatteries with high surface area electrodes that will not compromise overall device footprint is a fundamental aspect of the research towards smart integrated microsystems.

The objective of this research is the design, fabrication and characterization of a high surface area microbattery fabricated with MEMS technologies. The device consists of nanostructured cathodes using the *Tobacco mosaic virus* (TMV) as a template for the fabrication of a high surface area nickel electrode within a nickel-zinc battery. Self-assembly and metallization of the biological nanostructure will be integrated with traditional MEMS fabrication processes and a novel nickel-zinc microbattery will be developed using this technology. The effect of the increase in reactive area by the addition of the virus will be investigated through electrochemical characterization of the microfabricated devices and comparison of their performance with configurations that use planar nickel electrodes.

1.2 Device Overview

The microbattery developed in this work is a proof-of-concept device fabricated in a "parallel-plate" configuration as shown in Figure 1.2. The bottom layer is the cathode that consists of nickel coated TMV nanostructures and the top layer is a machined zinc plate which serves as the anode. The cathode layers are assembled on a gold film on a silicon wafer, where a thick SU-8 layer is fabricated using photolithography to define the device active area, electrolyte cavity and electrical connections, in addition to electrically isolating the two electrodes. The final device is assembled through adhesive bonding of the two layers with a thin SU-8 film.

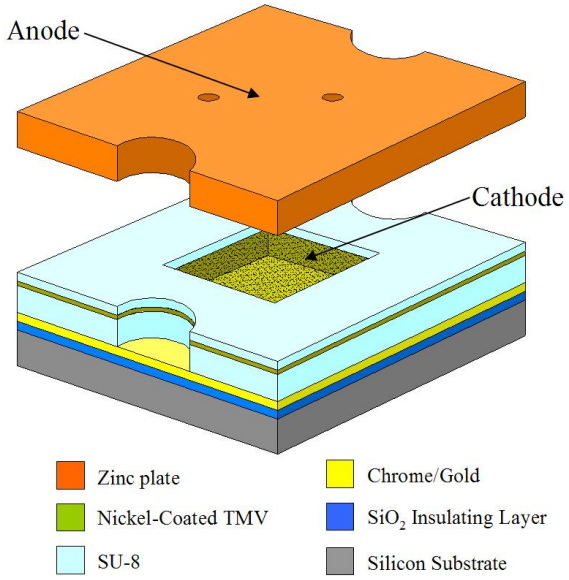

Figure 1.2: Three-dimensional view of the microbattery device.

Unlike most of the MEMS-fabricated batteries reported, introduction of the aqueous electrolyte in this device (1 molar potassium hydroxide) is performed after full device assembly through holes machined in the zinc and a novel plastic microfluidic package that was developed for this study. Electrochemical characterization of the full cell is performed using a potentiostat, which charges and

discharges the battery for repeated cycles of operation, while data is recorded using a commercial analysis software. Using this equipment, the charge-discharge behavior showing the progress of voltage versus time can be extracted and the capacity (the product of the current and the discharge time) can be successively calculated.

1.3 Review of Related Work

This section provides insight to fabrication processes and techniques related with the development of the microbattery presented in this work, as well as a review of previous and continued research in the field of MEMS fabricated energy storage devices and novel approaches for the development of high surface area electrodes.

1.3.1 MEMS Fabricated Batteries

Initial work in the field of MEMS fabricated batteries was focused on the development of planar (thin film) electrode designs using traditional micromachining processes. Lee *et al* demonstrated a disposable microbattery in a parallel-plate configuration with a zinc anode and a gold cathode [5]. The microbattery was fabricated with surface micromachining techniques and adhesive bonding and was activated with a droplet of electrolyte (sulfuric acid or potassium hydroxide) inserted between the two plates. Another non-rechargeable battery that uses an aluminum anode has also been demonstrated [6]. Humble *et al* fabricated and characterized nickel zinc microbatteries with electroplated active materials in a side-by-side configuration [7]. The device walls were made of SU-8 and the whole assembly was

sealed with paraffin or plastic after electrolyte insertion. Testing of this battery was performed both for low and high current density conditions to investigate its potential in powering wireless sensor communications. Singh *et al* combined this developed microbattery with a microfabricated solar cell array and electronics for charge control on a PCB board to demonstrate the feasibility of a hybrid power supply [8]. Batteries that do not use the typical acidic or alkaline but more environmentally friendly electrolytes have been reported. Sammoura *et al* developed water-activated batteries using MEMS technologies [9] and Lee presented cells operating with bio-fluids and fabricated using a plastic lamination process [10]. While the aforementioned cells use aqueous electrolytes, researchers have also developed lithium based thin-film batteries using a lithium phosphorous oxynitride (LiPON) electrolyte [11, 12]. Representative examples of these technologies are depicted in Figure 1.3 and their performance characteristics are summarized in Table 1.

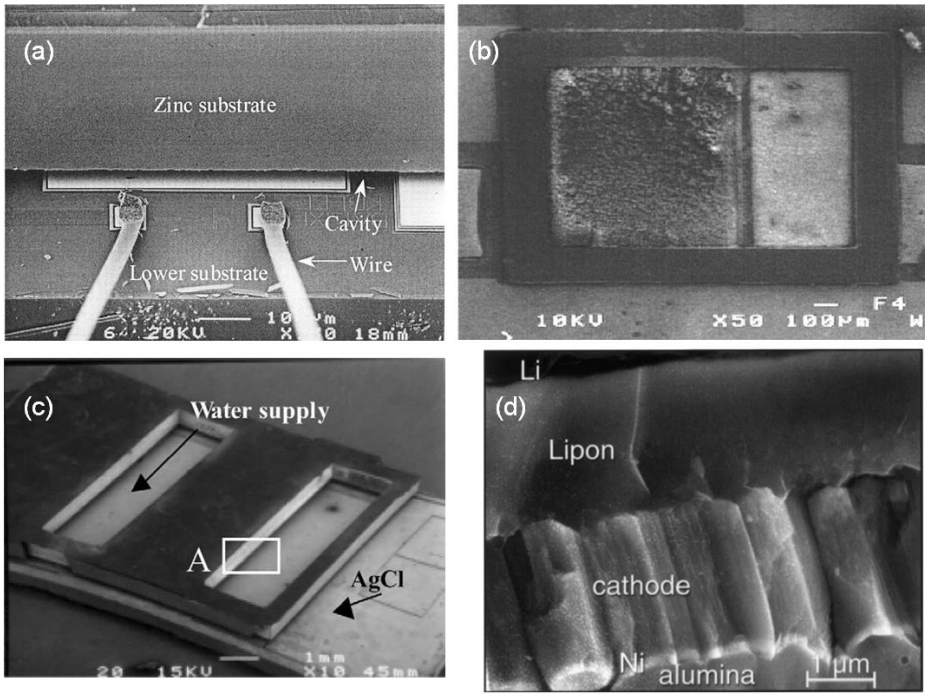

Figure 1.3: SEM images of (a) the disposable battery presented in [5], (b) the nickel-zinc battery of [6],with the nickel electrode on the left and the zinc electrode on the right, (c) the water-activated battery of[8] and (d) the solid-electrolyte battery layer arrangement of [11].

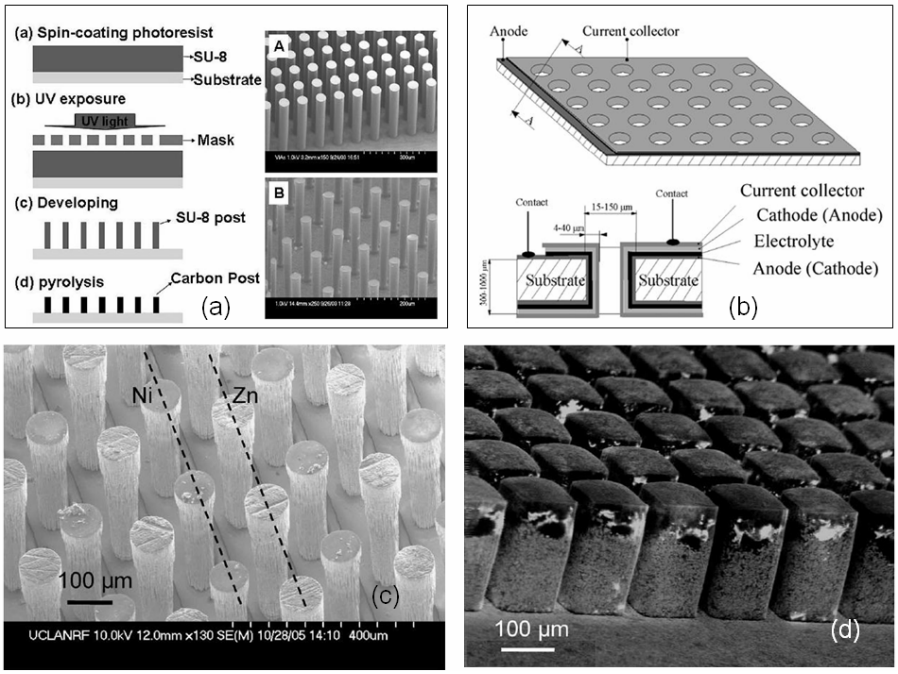

Figure 1.4: Schematic representation of the lithium-based batteries presented in [13] and [25] respectively (a-b) and SEM images of the microposts of [14] for nickel-zinc and lithium-ion batteries (c-d).

In addition to thin-film approaches, microfabrication techniques have also been used to create three-dimensional microbatteries. In these architectures, the electrodes have high aspect ratio out-of-plane microstructures, resulting in increased surface area while maintaining device footprint. Long *et al* [4] presented a review of this technology and emphasized on the benefit it provides to cover the energy requirements for wireless sensor network applications. Wang *et al* demonstrated the use of carbon electrodes made of pyrolized SU-8 microposts [13] (fig. 1.4(a)), while Nathan *et al* fabricated high surface area three-dimensional electrodes with a solid electrolyte on perforated silicon and glass substrates [44] (fig. 1.4(b)), both for lithium-based batteries. A novel fabrication process of high aspect ratio posts that uses molding in silicon and electroplating or colloidal processing was employed by

Chamran *et al* [14] for the development of nickel-zinc (fig. 1.4(c)) and lithium-ion batteries (fig. 1.4(d)). A novel three-dimensional battery

configuration has been suggested by Notten et al [18]. This approach makes use of the excellent intercalation chemistry of silicon for the development of CMOS compatible batteries in bulk silicon, however quantitative results have not been reported yet. A summary of these electrochemical cells is also given in Table 1.

TABLE 1 – SUMMARY OF MEMS FABRICATED BATTERIES

Author/Institute	***Electrode Structure***	***Electrolyte***	***Battery type***	***Voltage***	***Capacity***	Fabrication
Lee *et al* [5], UC Berkeley	Zn (anode)-Au (cathode)	Sulfuric acid/hydrogen peroxide or potassium hydroxide	Non-rechargeable	1.5 V	4.88 mAh/cm^2	Surface micromachining, adhesive bonding
Cardenas-Valencia *et al* [6], University of South Florida	Al (anode) – Pt (cathode)	Sodium hydroxide/potassium chloride/hydrogen peroxide	Non-rechargeable	0.6 V	70 mAh/cm^2	Aluminum lines patterned over dielectric on platinum
Humble *et al* [7], BYU	Ni (cathode)-Zn (anode)	Potassium hydroxide	Rechargeable	1.7 V	0.322 mAh/cm^2	Electroplated materials, polymer walls
Sammoura *et al* [9], UC Berkeley	Mg (anode) – CuCl or AgCl (cathode)	Water	Non-rechargeable	1.65 V	0.78 mAh/cm^2	Adhesive bonding, through-etch holes, sputtered films
West *et al* [11], JPL-Caltech	$LiCoO_2$ (cathode) – Ni (anode)	Lithium phosphorous oxynitride (LipON)	Rechargeable	3.9 V	10 μAh/cm^2	Sputtering and evaporation of solid films
Wang *et al* [13], UC Irvine	Carbon (anode) – Li (cathode)		Rechargeable	3 V	0.125 mAh/cm^2	Pyrolisis of SU-8 posts, commercial cathodes
Nathan *et al* [44], University of Tel Aviv	MoO_yS_z (cathode) – lithiated graphite (anode)	Hybrid Polymer Electrolyte (HPE)	Rechargeable	2.2 V	2 mAh/cm^2	Deposition of thin films on the walls of perforated substrates
Chamran *et al* [14], UCLA	Ni (cathode)-Zn (anode)	Potassium Hydroxide	Rechargeable	1.7 V	2.5 μAh/cm^2	Interdigitated Ni-Zn posts by electroplating

1.3.2 Nanostructured Batteries and Electrodes

To further increase reactive surface area, the integration of nanomaterials and biological nanostructures in battery electrodes has also been investigated. The bulk of this research has been focused on developing novel materials using various deposition techniques for lithium-ion batteries [16-18], however, more chemistries are being explored [19]. In the field of nickel-zinc batteries, the use of zinc oxide (ZnO) nanorods has been shown to increase reactive surface area compared to conventional zinc oxide and improve cycling performance [20] and novel nickel hydroxide ($Ni(OH)_2$) hexagonal nanostructures have been found to significantly boost the energy density of alkaline-based batteries (fig. 11(a)) [21]. While most of these activities have been limited to the characterization of the individual electrodes, Pushparaj *et al* fabricated flexible light-weight batteries using nanoporous cellulose paper and embedded carbon nanotubes (fig. 1.5(b)) [22].

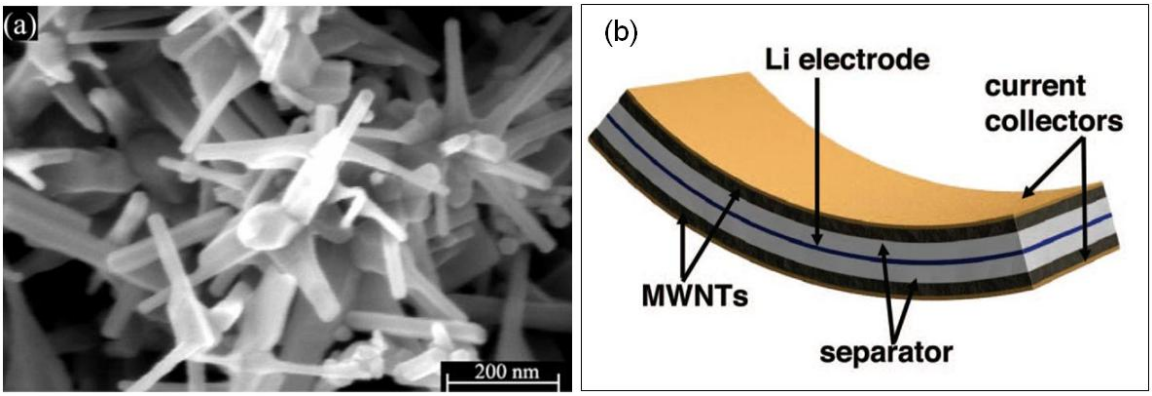

Figure 1.5: (a) SEM image of as-prepared ZnO nanorods [20] and (b) schematic representation of a flexible energy storage device [22].

The use of biological nanomaterials is an attractive approach for the fabrication of battery electrodes without complex deposition techniques, as they exist

in nature as high aspect ratio nanostructures and they can be modified to attach to substrates of interest and bind to a variety of active battery materials. Cobalt oxide and hybrid gold-cobalt oxide nanowires based on engineered modifications of the M-13 bacteria virus have been synthesized based on amino-acid interactions and used as positive electrodes in a macroscopically assembled lithium-ion battery [23]. The performance of these electrodes was superior to that of electrodes without the virus, demonstrating the advantage of this technology. Previous work by Royston *et al* reported the use of genetically modified *Tobacco mosaic virus* (TMV) as a template for electroless deposition of cobalt and nickel [24]. An order of magnitude increase in surface area was estimated for the nanostructured nickel materials and their potential as battery electrodes has been demonstrated through electrochemical experiments. Figure 1.6 shows images of these nanostructured viral electrodes.

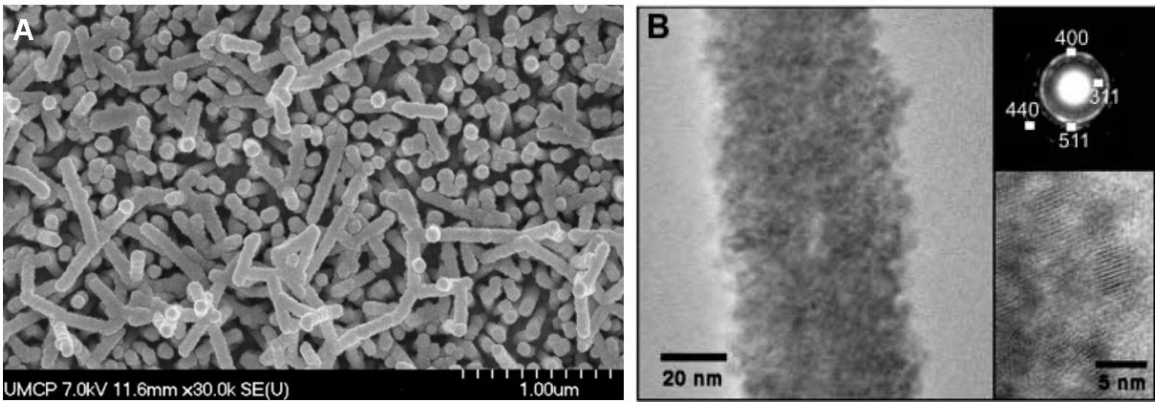

Figure 1.6: (a) SEM image of a nickel coated TMV electrode [24] and (b) TEM images of a cobalt oxide M-13 viral nanowires [23].

1.3.3 Microgenerators and Fuel Cells

Besides electrochemical cells (batteries and fuel cells), several other approaches have been examined for micro-scale energy conversion, most of which

are based on four transduction mechanisms: electrostatic, electromagnetic, piezoelectric and thermoelectric. Electret-based generators have been fabricated using micromachining techniques [25], resulting in power generation in the mW range. Electromagnetic rotary microgenerators have been successfully developed by Arnold *et al* [26]. The maximum reported power by these machines was notably higher (in the order of W), nonetheless with a complex fabrication process. Piezoelectric generators based on harvesting of ambient vibrations using diaphragms and suspended microstructures have been demonstrated and produced power densities comparable to those of lithium ion batteries [27, 28]. A thermoelectric generator with Cu-Ni electroplated thermolegs in an SU-8 mold has been presented by Glatz *et al* [29] and was recently optimized to produce power in the order of several hundreds of $\mu W/cm^2$ [30]. Figure 1.7 shows schematic representations and images of such micromachines.

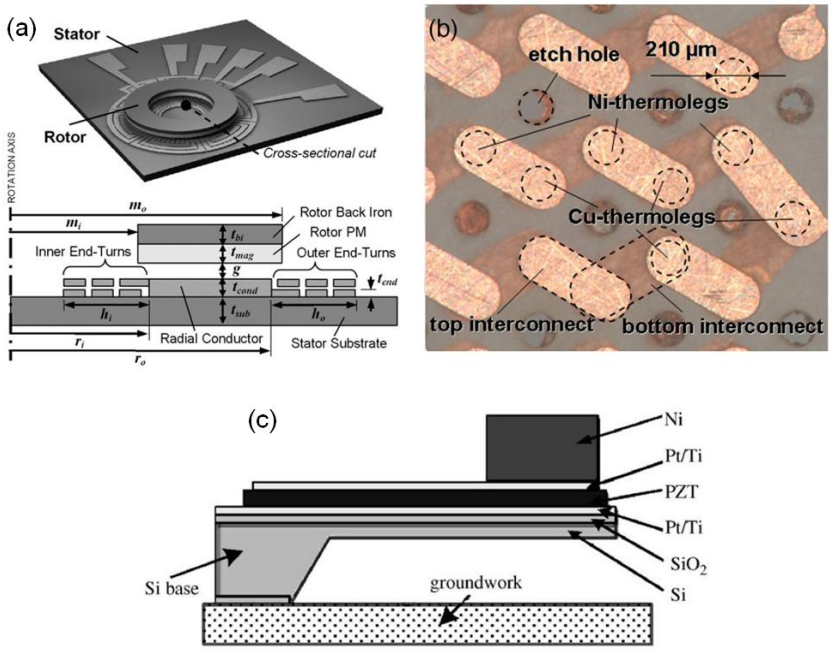

Figure 1.7: (a) Schematic of the electromagnetic generator described in [26], (b) image of the thermoelectric generator structure of [29] and (c) cross-sectional view of a cantilever for piezoelectric energy harvesting [30].

A fuel cell is an electrochemical conversion device that constantly uses fuel (hydrogen) and oxidants to produce electricity. It has become a technology of particular interest because of the "clean" nature of the chemical reactants and byproducts. Miniaturization of fuel cells is a very important issue for the realization of commercially available devices and this challenge has been addressed by MEMS researchers. Polymer exchange membrane (PEM) fuel cells have been reported [31, 32] , while other types of cells such as micro-direct methanol fuel cells [33], solid oxide fuel cells [34] and bio-photosynthetic fuel cells [35] have also been studied, often employing high surface area designs for the catalytic surfaces (fig. 1.8(a-b)). In addition to the electrode, catalyst and membrane structure development, research is also being conducted to miniaturize components such as fuel reformers and reactors for decomposition of fuel to hydrogen [36, 37], which are very important building – blocks for the system-on-a-chip level integration of fuel cells for portable power applications (fig 1.8(c-d)).

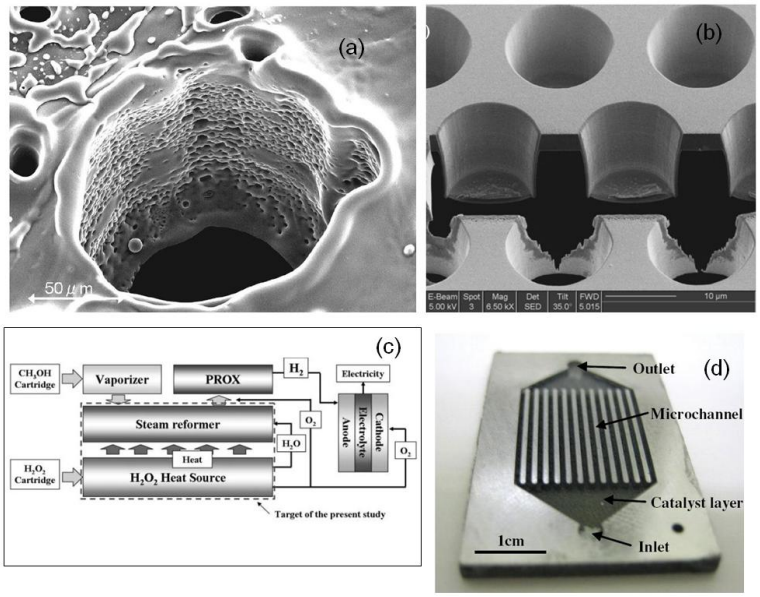

Figure 1.8: (a) SEM image of a high surface area carbon electrode for a bio-synthetic fuel cell [35], (b) high surface area microfabricated structures for a solid-oxide fuel cell [34], (c) schematic representation of fuel reformer [36] and optical image of a fuel cell microreactor [37].

1.3.4 Electroless Plating

Electroless plating is a chemical deposition technique in which the metal coating is achieved without the use of an external power supply and the electrons required for the reduction on the target substrate are provided by a chemical reaction in the solution. Unlike electrodeposition where the thickness and grain size are primarily a function of the current density, in this method the plating rate depends on more parameters, such as the concentration of the solution, the pH and the plating temperature. Electroless plating can be classified under three categories [38]:

1) Deposition by ion or charge exchange (displacement reaction, immersion plating)
2) Deposition by immersing the plating metal in a metal salt solution and bringing it in contact with another piece of metal, and,
3) Deposition of the metal from solution containing reducing agents (typically on catalyzed surfaces).

The latter method is the most commonly used and it is also the focus of this work. In this process, the electrons required to reduce the metal ions on the target surface are provided by a reducing agent R^{n+}. The reactions that take place on the catalytic surface are shown below:

$$R^{n+} \rightarrow R^{(n+z)} + ze$$

$$Me^{z+} + ze \rightarrow Me$$

where M represents the metal, z the number of electrons released and $R^{(n+z)}$ are the oxidized products.

In the field of MEMS, electrochemical deposition in the form of electroplating remains the most commonly encountered method for creating thick metallic structures. Electroless plating however offers some significant advantages such as lower cost, uniform deposition, versatility in the use of materials as it does not require conductive substrates and simplified fabrication as it is performed by immersion in a chemical solution [39]. Nickel electroless plating has been used extensively for the remetallization of aluminum bond pads in IC circuits [40, 41]. Gold and nickel layers for sensor surface functionalization and battery current collectors respectively have also been demonstrated [42, 43]. In addition to these applications, this deposition process has been used for the fabrication of multilayer structures through laser-assisted plating for 3D MEMS applications [44] and the development of magnetic structures using rare earth plating materials [45], something that cannot be achieved with conventional electroplating (fig. 6).

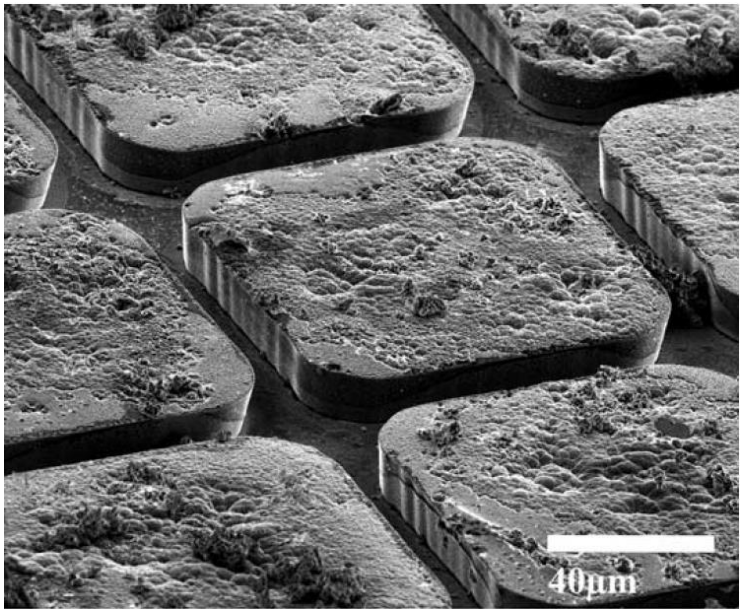

Figure 1.9: Magnetic structures fabricated using electroless plating of rare-earth metals [45].

1.3.5 Fabrication and Bonding with SU-8

SU-8 is a negative-tone epoxy-resin photoresist that was originally developed and patented by IBM in 1989 and introduced into MEMS fabrication in the mid-90s. Due to its low optical absorption in the UV range and the different viscosities in which it can be synthesized, SU-8 is a very common material of choice for high resolution photolithography, with aspect ratios higher than 10:1 [46] and structural thicknesses varying from a few microns up to 2 millimeters. Wang *et al* [47] fabricated SU-8 microposts with a thickness of 200 μm and aspect ratio > 10:1 in a single spin-coating step, while Mata *et al* [48] demonstrated polymer microstructures with thicknesses up to 540 μm and feature size of 10 μm using a multilayer process based on alternating layers of thin and thick SU-8 (Fig. 1.10).

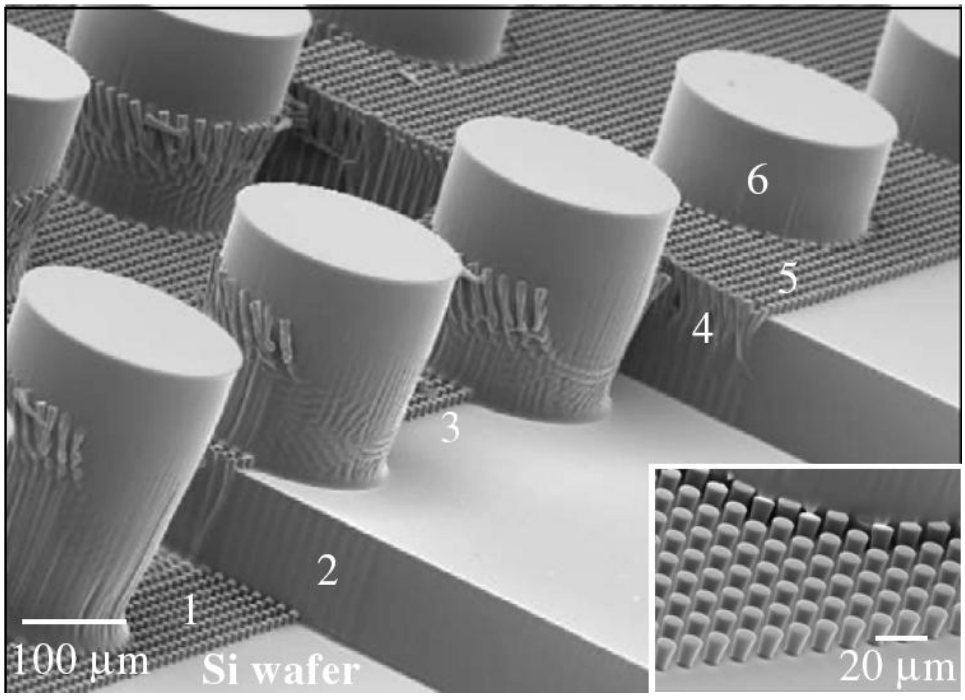

Figure 1.10: SEM image of a six-layer SU-8 microstructure fabricated using the process described in [48]. Each layer is numbered in the order it was patterned.

An attractive application for the SU-8 photoresist is related with metallization of thick structures in a low-cost "LIGA-like" process. Briefly, a seed metal layer is patterned on a substrate followed by the polymer lithography which creates a thick mold. This mold is then filled with the target material using electrochemical deposition and it is finally removed by means of various techniques. Arnold *et al* fabricated rotors for magnetic induction machines using an SU-8 mold which was then mechanically removed from the silicon substrate [49]. Ghantasala *et al* [50] demonstrated the use of laser ablation for mold removal while Song *et al* [51] reported free-standing metallic structures with SU-8 molds and sacrificial photoresist layers (Fig. 1.11). Recently, the SU-8 manufacturer has commercialized a new product (Omnicoat) which can be spun on the wafer before SU-8 lithography, patterned before development and then lifted off in TMAH after electroplating [46].

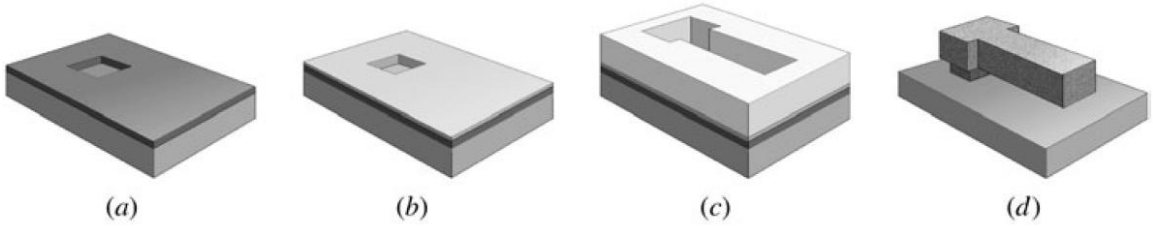

Figure 1.11: Use of SU-8 for electroplating with a photoresist sacrificial layer: (a) the sacrificial layer is patterned, (b) seed layers are deposited, (c) the SU-8 mold is created and (d) the free-standing structure is released [51].

In addition to this versatility and simplicity in fabrication, several other unique properties of this polymer, such as biocompatibility, index of refraction, transparency and Young's modulus make SU-8 lithography a widely used process in various MEMS applications. Micro channels with waveguides and laser structures for complex microfluidic systems have been fabricated, showing the advantages of the process for the realization of BioMEMS devices [52, 53]. An example of such a

system for lab-on-a-chip applications is shown in Figure 1.12, where a fluidic network is integrated with a dye laser and waveguides all made in SU-8 for optical sensing. Compared to silicon, SU-8 has lower stiffness with similar mechanical stability and this has inspired its use in the fabrication of suspended structures such as cantilevers and micro mirrors (Fig. 4a) that can be actuated at lower voltages [54, 55].

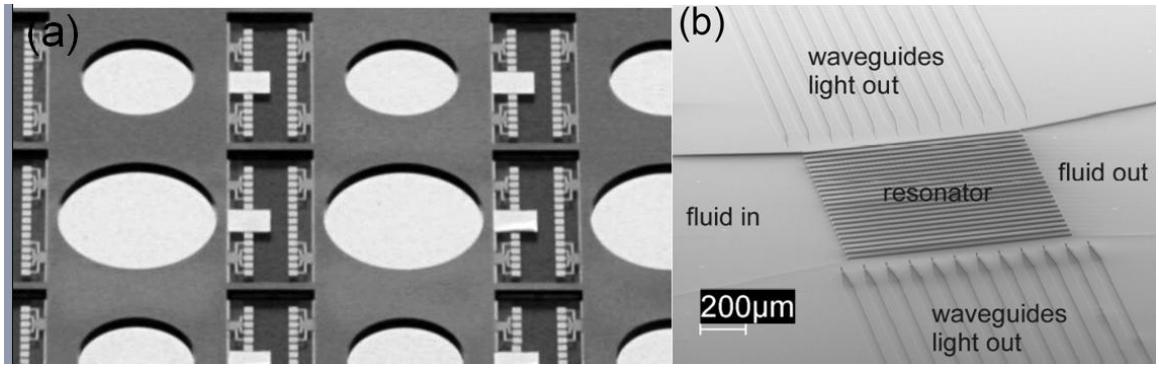

Figure 1.12: (a) Polymer micromirrors fabricated in SU-8 [55] and (b) a microfluidic system made in SU-8 containing waveguides, a laser resonator and microfluidic channels [52].

The processing parameters of SU-8 allow its application in low-temperature polymer bonding, also referred to as adhesive bonding. This type of bond lacks in mechanical stability and does not result in hermetically sealed structures like fusion or anodic bonding, but the tolerances are acceptable for several microfluidic and packaging applications. The most commonly encountered method for bonding with SU-8 makes use of a thin layer spun on a pyrex wafer, which is then aligned and pressed against another structural SU-8 layer on a separate wafer [56, 57, 58]. This procedure has the advantage that a flood exposure is possible through the pyrex wafer after the two layers have been bonded, which cross-links the polymer and strengthens the bond. Bonding has also been achieved without the use of such a blanket exposure through transparent substrates. Blanco *et al* [59] achieved the fabrication of three

dimensional microfluidic structures through bonding of SU-8 layers on silicon wafers in a wafer bonder. Figure 1.13 shows a schematic representation of this process. After full lithographic patterning of the structures in both substrates, the two wafers are brought in proximity under a wafer bonder, heated to a moderate temperature and then pressed and held together with the substrates heated to a temperature higher than the glass transition temperature of the polymer.

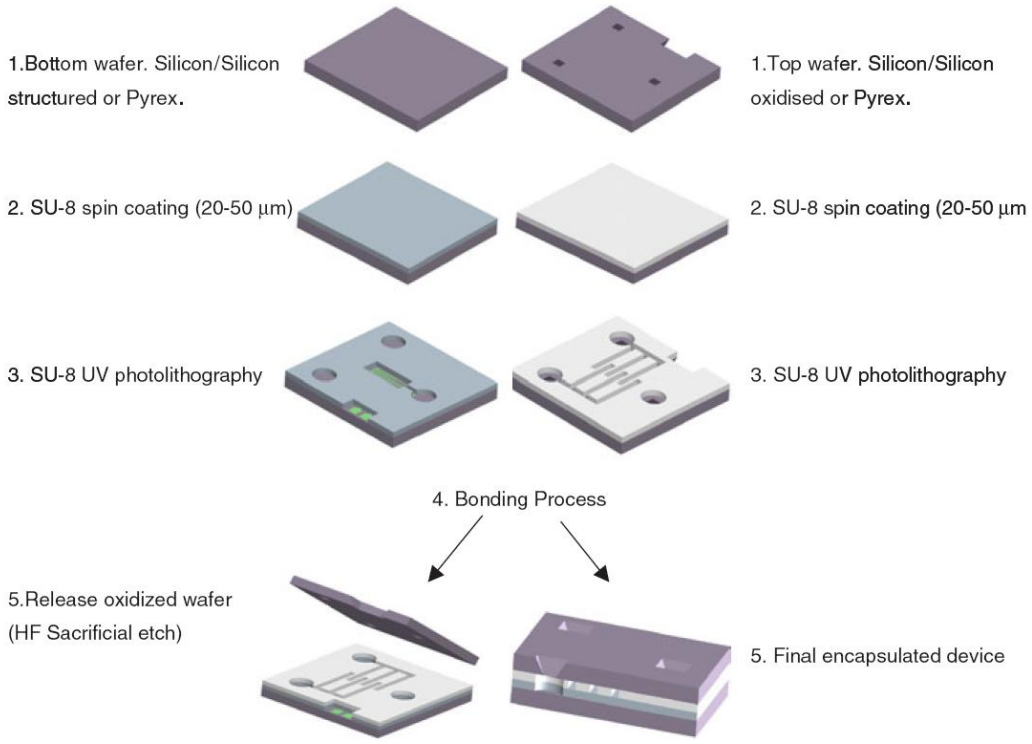

Figure 1.13: Schematic representation of the fabrication process described in [59] for the fabrication of multi-layer fluidic networks in SU-8.

1.4 Thesis Contributions and Outline

As mentioned in the previous section, the use of nanostructured electrodes and biologically inspired materials for battery applications was mostly explored through electrochemical characterization of the half-cell devices. This thesis presents the first

successful demonstration of a MEMS-fabricated battery utilizing viral nanostructures with the following specific contributions:

a) The TMV self-assembly and nickel coating process were incorporated as a fabrication step for the development of a nickel-zinc microbattery.
b) The first prototype device was extensively characterized to investigate cycling and device design parameters and its performance was compared to a similar device with a planar nickel electrode.
c) The performance of the TMV modified device was found to be greater by a factor of six during the initial discharge.
d) Demonstration of photolithographic patterning of the TMV shows its great potential for batch fabrication of MEMS high-surface-area devices using this technology.

Chapter 2 of this thesis provides some fundamental background on battery operation and electrochemistry concepts and discusses aspects of the nickel-zinc battery system. Chapter 3 focuses on the Tobacco mosaic virus, showing its use in various applications with an emphasis on the development of nanostructured materials. Chapter 4 presents the design and fabrication process of the device developed in this work, while chapter 5 shows the testing apparatus and the results of the electrochemical characterization.

Chapter 2: Fundamental Concepts of Electrochemistry

This chapter discusses fundamental concepts of electrochemical conversion. The building block components of batteries are presented, Figure s of merit and battery models are analyzed and design considerations as well as important parameters of operation are discussed.

2.1 Electrochemical Cell

The electrochemical cell is the building block component of batteries which are in practice comprised of arrays of such cells in series or in parallel. An electrochemical cell is a device that converts the chemical energy stored in its active materials to electricity by means of oxidation and reduction reactions (redox reactions). An oxidation reaction involves the release of electrons by an atom, molecule or ion while a reduction reaction described the gain of electrons. This type of cell consists of three components:

1) *The anode or negative electrode*. This is the electrode that is oxidized during operation and releases electrons to an external circuit.
2) *The cathode or positive electrode*, which accepts these electrons allowing reduction to occur.
3) *The electrolyte*, which is the medium for transfer of electrons in the form of ions within the cell from the anode to the cathode. It can be a liquid such as a metal salt or acid; however, batteries with solid polymer electrolytes have also been presented.

The anode and cathode materials are selected based on several criteria. They have to be good reducing and oxidizing agents respectively, offer high stability, good electrical conductivity, operating voltage and capacity as well as enable simple fabrication and assembly at low cost. The electrolyte on the other hand must satisfy the basic requirement of good ionic conductivity and poor electrical conductivity so that the battery electrodes will not be short-circuited. Additionally, ease of handling, safety of operation and environmental concerns have to be taken into account. In commercial batteries, an ion-permeable separator is often used to mechanically separate the anode and cathode.

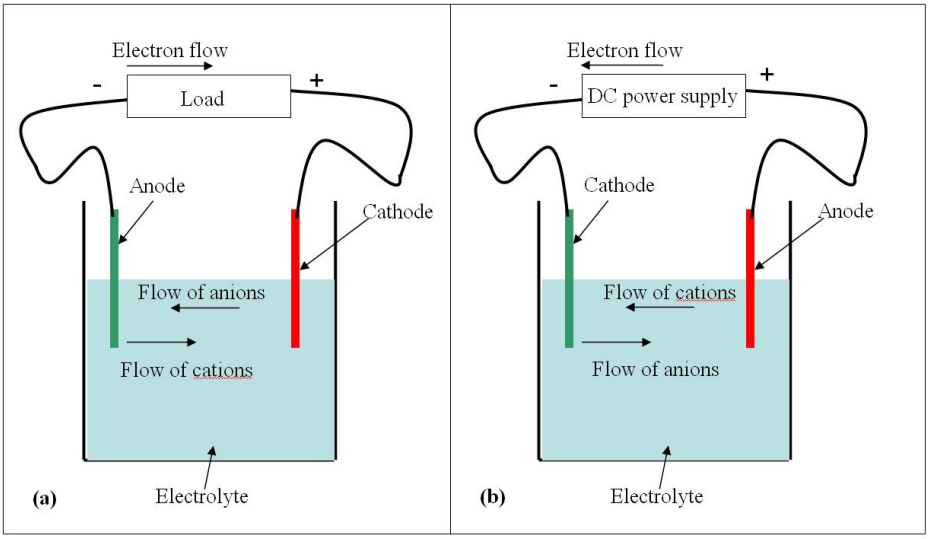

Figure 2.1: (a) Discharge mode of operation (b) charge mode of operation

A battery can operate in two conditions, the discharge mode and the charge mode. These are schematically illustrated in Figure 2.1. When the cell is connected to an external load, electrons flow from the anode, which is oxidized, to the cathode, which accepts the electrons and is reduced. The circuit is completed in the electrolyte by the flow of negative ions to the anode and positive ions to the cathode. During the charging operation, DC current is provided by a power supply and the flow of the

species is reversed. Since by definition the anode and cathode are the electrodes that are oxidized and reduced respectively, in this mode, the positive and negative electrodes are now interchanged.

2.2 Performance Parameters

This sub-section provides an overview of the most critical battery performance parameters the operating voltage and battery capacity, which define what electrochemical system should be used in applications with specific requirements.

2.2.1 Battery Voltage

The theoretical voltage of a battery is controlled by the standard electrode potentials of the active materials. The standard electrode potential is a measure of the reactivity of the material and it corresponds to the electrical potential measured at standard conditions, where all solutions are at concentrations of 1mol/kg and gases are at a pressure of 1 bar. While the electrical potential between two electrodes can be measured effectively, accurate measurement of one electrode potential is not an easy task. On that note, the electrode potentials are measured with regards to a reference electrode. This is the Standard Hydrogen Electrode (SHE) whose potential has been set upon convention to be 0.0 V. Since for a redox reaction the oxidation potential is the negative of the reduction potential, it is sufficient to measure one of these two

voltages. In the case of the standard electrode potential, the reduction potential is the one commonly used.

Based on these definitions, the theoretical voltage of an electrochemical cell is taken as the sum of the anode and cathode potentials, where the oxidation potential is the negative of the reduction value:

$$E^0_{cell} = E^0_{anode} + E^0_{cathode} \qquad (1)$$

For example, for the commercial nickel-zinc battery the reactants are zinc (anode) and NiOOH (cathode). The potentials for these two materials are -1.24 V and 0.49 V respectively, using standard electrode potential tables [60]. The operating voltage for this chemistry will then be 1.73 V. This is also the expected value of the open circuit voltage, which appears if both electrodes are fabricated in the charged state and no load is connected between the battery terminals.

2.2.2 Battery Capacity

The capacity of a battery, as defined by Linden [60], is the total quantity of electricity involved in the electrochemical reaction. It corresponds to the amount of charge released from the active materials during the discharge operation and it is expressed in Coulombs, or more commonly in Ampere-hours. Theoretically, 1 gram-equivalent weight of material will deliver 96,587 C or 26.8 Ah. This quantity is represented by F and is called “one Faraday” [5]. The 1 gram-equivalent weight is the molecular weight divided by the number of electrons involved in the reactions. The capacity can be therefore calculated using the equation:

$$Capacity = \sum \frac{nF}{weight\_of\_reactive\_components} \qquad (2)$$

where n is the number of electrons released in the reaction and F is Faraday's number. As an example, consider the reaction occurring in a nickel-zinc battery:

$$2NiOOH + Zn + 2H_2O \leftrightarrow 2Ni(OH)_2 + Zn(OH)_2$$

The number of electrons released in the discharge reaction is 2 and the molecular weight of the reactants is 183.356 g and 65.37 g respectively. Using the above equation, the theoretical calculated capacity for this system would be 0.215 Ah/g.

Another way to consider capacity is in an energy basis, by multiplying the calculated quantity of electricity with the battery operating voltage. This results in the gravimetric energy density E_g, expressed as:

$$E_g = Capacity \times E_{cell}^0 \qquad (3)$$

For the system examined previously, using the results of equations (1) and (2), the gravimetric energy density is calculated to be 0.372 Wh/g.

The small size of MEMS fabricated batteries as well as the amounts of materials used makes the process described above in determining the battery capacity less attractive. In these cases, the Figure of merit that is normally used is the normalized quantity of electricity over the area or volume of the device. This is expressed in Ah/cm^2 or Ah/L and is a more representative way to characterize the performance of a microscopic electrochemical cell.

2.3 Classification of Batteries

Electrochemical cells and batteries are divided into two major categories, primary (non-rechargeable) and secondary (rechargeable), depending on their ability to be electrically recharged by reversing the direction of current. Primary batteries are a relatively inexpensive and lightweight source of portable energy. The general advantages that they offer are good shelf life, high energy density at low to moderate discharge rates and little maintenance requirements. Zinc has been so far the most popular material of choice for non-rechargeable batteries due to its low cost, compatibility with aqueous electrolytes and reasonably good shelf life. Commonly used zinc-based systems include zinc-air, silver-zinc and zinc-carbon (Leclanche) batteries. In addition to zinc, magnesium has similar properties that have enabled its use in primary batteries, while aluminum has also been considered due to its high electrochemical potential.

Secondary batteries are used both as power sources when cost saving is required (e.g. electric vehicles) as well as energy-storage devices. In this case they are charged by a source of energy such as light and then they can deliver this energy on demand to any load that is attached to their terminals. They exhibit high power densities and high discharge rates, flat discharge curves, and good low-temperature performance. Compared to primary batteries, they have lower energy densities and poorer charge retention; however, any lost capacity can be restored by recharging the device. Rechargeable batteries of particular interest are lithium-ion, lead-acid and nickel-based (nickel-metal hydride, nickel-cadmium and nickel-zinc) batteries.

2.4 Analysis and Design

2.4.1 Battery Model

Ideally, the battery would operate constantly at its theoretical voltage and would release all the stored chemical energy into electricity until the active materials were depleted. In practice however, there are losses due to polarization when a load current passed through the electrodes. These losses are caused by three effects:

1) *activation polarization*, which drives the electrochemical reaction at the electrode surface,
2) *concentration polarization*, which occurs due to concentration differences of the reactants and products at the electrode surface and in the bulk, as a result of mass transfer, and,
3) *Ohmic polarization*, due to the internal resistance of the cell, which is proportional to the current drawn from the device.

These losses consume part of the energy, which is given off as waste heat. While activation and concentration polarization can be calculated from theoretical equations if the parameters are available, it is difficult to determine these quantities in practice because of the complicated physical structure of the electrodes and the overall cell composition. The ohmic losses are the sum of the ionic resistance of the electrolyte, the electrical resistances of the active mass, electrodes and current collectors, and follow a linear relationship according to Ohm's law. When the battery is connected to an external load *R*, its working voltage will be given by:

$$V = E_{cell}^{0} - (E_{ct,a} + E_{c,a}) - (E_{ct,c} + E_{c,c}) - IR_i = IR \qquad (4)$$

where the first term is the open-circuit voltage of a cell, $E_{ct,c}$ and $E_{ct,a}$ are the activation polarizations at the anode and cathode respectively, $E_{c,a}$ and $E_{c,c}$ are the concentration polarizations at the anode and cathode, I is the operating current and R_i is the internal resistance of the cell. The relationship between the cell voltage and the polarization for increasing current values is shown in the graph of Figure 2.2. It can be observed in this graph that the effects of polarization are small for small current values, while at higher rates the *IR* loss becomes the dominant factor and affects the performance of the device.

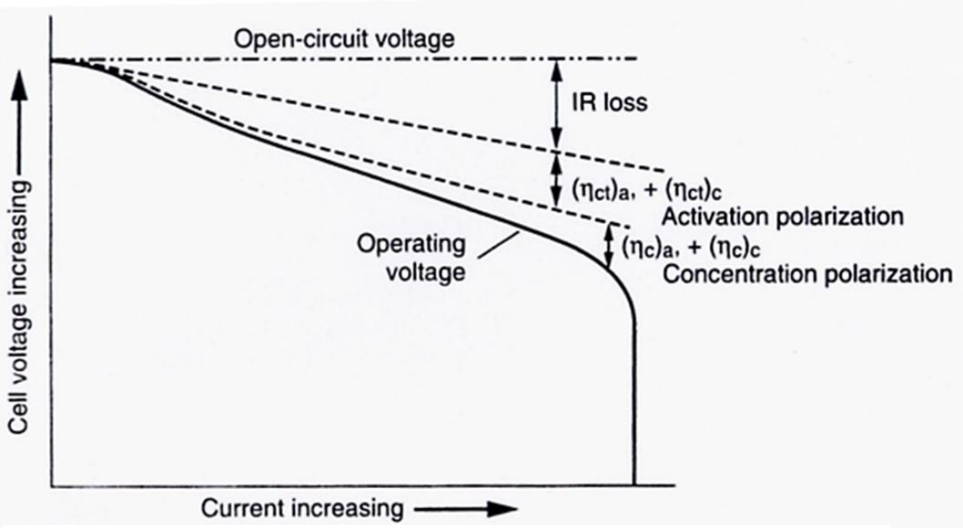

Figure 2.2: Cell polarization as a function of operating current [61].

Several steps can be taken to reduce the effect of polarization losses. The electrolyte salt and solvents should have chemical stability to avoid reaction with the active materials and their conductivity has to be high enough to exceed the IR polarization. The use of high surface area electrodes reduces the charge transfer polarization by reducing the local current density for a given total operating current and increasing the mass transport through the ionic conductor, thus preventing excessive mass build-up. Additionally, the current collector materials should be

selected in a way that possible contact with the electrolyte will not cause corrosion problems.

2.4.2 Voltage Levels

The voltage of an electrochemical cell has several reference points. As defined previously, the open circuit voltage is the theoretical value predicted by the chemistry of the system in use. The nominal voltage is the voltage that is generally accepted as typical during the operating process, while the working voltage represents the value when the battery is connected to an external load. The midpoint voltage is the average value of the discharge curve and the end voltage is considered to be the lower limit where the battery has delivered most of its capacity. The discharge curves also vary from system to system for a practical battery. Typical examples are shown in Figure 2.3 Curve 1 represents a discharge that is close to the ideal “step-like” operation, where the effect of the losses is minimal until the active materials are depleted. Curve 2 is typical of two-step discharge indicating a change in the reaction mechanism and potential of the active materials and it is expected in cases where two chemical reactions appear. Finally, curve 3 illustrates a reaction where the composition of the active components as well as the effects of polarization change during one cycle of operation.

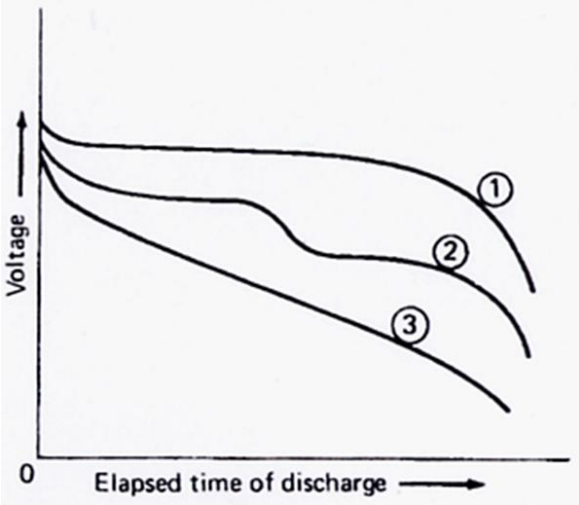

Figure 2.3: Cell polarization as a function of operating current [61].

During the charge part of the cycle, allowances have to be made for any lost capacity and the charge voltage should be slightly higher. A typical example is shown in Figure 2.4.

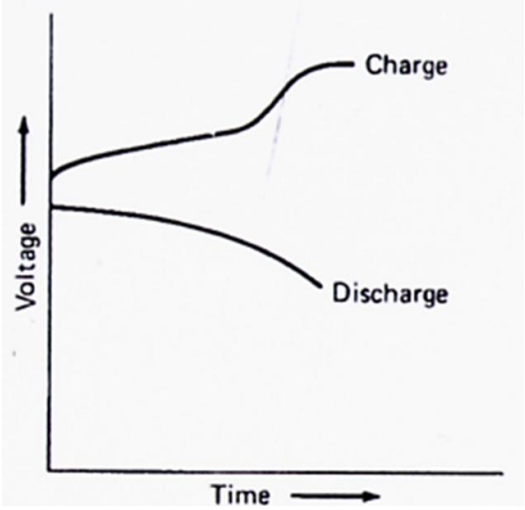

Figure 2.4: Typical voltage profile on charge and discharge [61].

2.4.3 Effect of temperature

The temperature of operation is also an important factor as it affects the capacity and voltage characteristics. This is due to the reduction in chemical activity

and the increase in internal resistance at lower temperatures. This is illustrated in Figure 2.5, where discharge curves for increasing values of temperature are presented (the curve at T4 represents a discharge at room temperature). While the internal resistance of a battery decreases with temperature, the chemical activity may become too rapid at elevated temperatures and cause a net loss in capacity. The optimum operating conditions for batteries have therefore been observed in the range of 20°C to 40°C.

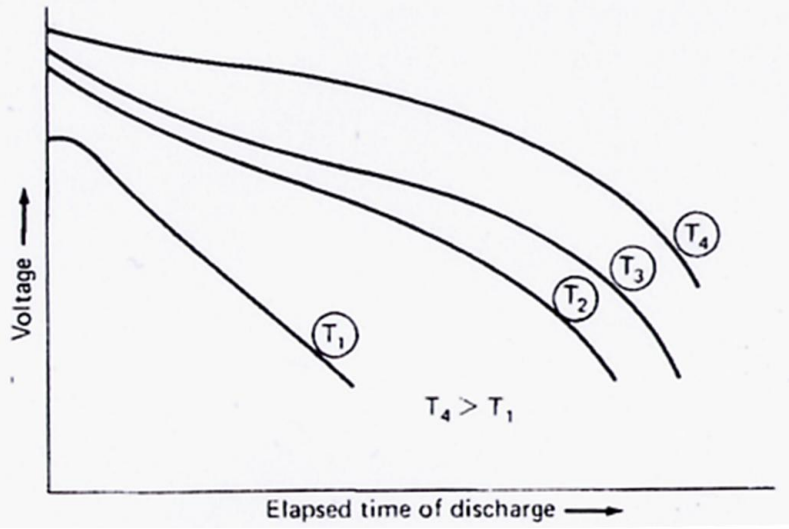

Figure 2.5: Effect of temperature in battery capacity [61].

Chapter 3: The *Tobacco mosaic virus* as a Nanoscale Template

Nanotechnology and the development of highly-ordered nanostructured materials in particular are widely increasing fields of research that promise to address the limitations of conventional semiconductor technologies in scaling beyond certain limits. Nanomaterials are key components for next-generation electronic devices as well as for biomedical, energy storage and catalysis applications. The most commonly used templates include porous membranes, fabricated nanoparticles and nanotubes [62]. These structures however are fabricated using expensive and energy-intensive equipment and the "top-down" approach employed in their processing often lacks in creating repeatable templates at the nanometer scale.

Biological nanotemplates, utilizing the "bottom-up" approach in which structures are constructed from atomic and molecular components through self-assembly, have emerged as a natural alternative to these processes. These systems offer unique advantages such as very high aspect ratios, batch production at low cost and the ability to genetically modify their structure and enhance their functionality as templates for a variety of applications. Among these templates, silk fibroin fibers, microtubules and DNA molecules have been functionalized with metals including iron, gold, platinum and palladium [62]. Viruses constitute another attractive approach for nanoscale fabrication as they are easy to manufacture, they show stability in environmental conditions, and their inherent aspect ratios (~132 for the M-13 bacteriophage and ~17 for the Tobacco mosaic virus [63]) allow structuring of high surface area materials.

This chapter presents an overview of the *Tobacco mosaic virus* (TMV) as a nanostructured template. The discussion emphasizes on the structure of the virus, the properties that make it useful in nanotemplate synthesis as well as the various genetic modifications and applications that have been previously demonstrated. This presentation shows the feasibility of using biological nanomaterials in the field of electronics and energy storage.

3.1 Structure

The TMV is a plant virus with worldwide distribution that has been studied since the end of the 19th century and has been found to infect approximately 200 plant species, including tobacco, tomato, and other crop plants [64]. It is one of the simplest and readily available viruses, and this attributes have been used in the understanding of several other virus systems. The TMV is a high aspect ratio cylindrical nanostructure, measuring 300 nm in length with an outer diameter of 18 nm and an inner diameter of 4 nm. Each TMV structure consists of approximately 2,130 coat protein subunits wrapped around a single-stranded positive-sense RNA in a helical structure. A positive-sense RNA can act as a viral messenger RNA that can be directly translated by the host cell. Figure 3.1(a) shows a TEM image of wild-type viruses while Figure 3.1(b) is a simplified model of the TMV structure.

The viral structure has been described clearly in [65]. The self-assembly of the virus results from finely balanced, orthogonal weak interactions between the protein molecules and the RNA. These interactions occur along the lateral as well as the longitudinal directions of the helix. The self-assembly proceeds in two stages:

nucleation and elongation. During the nucleation stage, the protein molecules assemble by hydrogen bonds and electrostatic and hydrophobic interactions into small disks (nuclei). During the elongation stage, these disks bind electrostatically, one at a time, to a hairpin loop in the RNA stand and they finally anneal into a single helical aggregate.

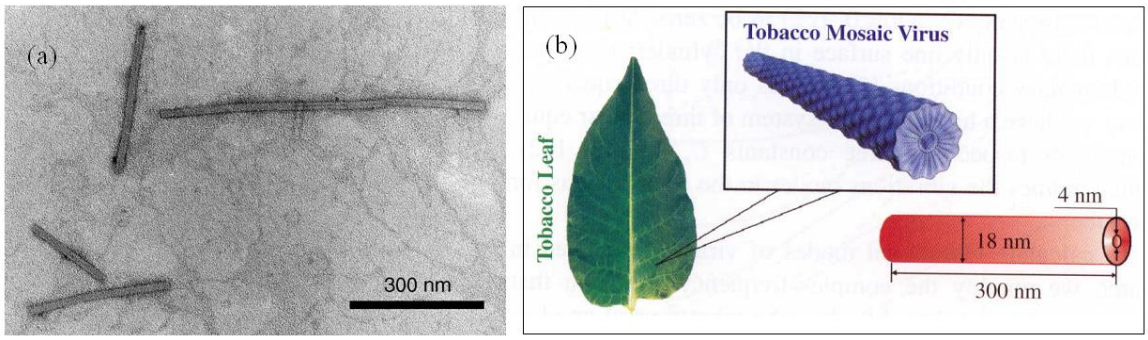

Figure 3.1: (a) TEM image of wild-type viruses, (b) simplified model of the TMV structure [63].

Wild-type TMV virions contain numerous electrostatic interactions demonstrated through repeatably exposed amino acids around their surface, which include arginine, lysine, aspartic and glutamic acids [66]. Amino acids can be hydrophobic or hydrophilic, polar or unpolar, or charged. Figure 3.2 shows a model of the amino acids around the TMV disk [67]. Hydrophilic amino acids are colored white, water molecules are colored blue, polar hydrophilic amino acids have a green color and the charged hydrophilic ones are red. These properties can influence the chemical behavior of the molecule. In the case of TMV, the accessible outer molecular surface of the virus is dominated by hydrophilic amino acids, of which a large part is charged. Hydrophobic amino acids can also be accessed; however, they are predominantly buried in a hydrophilic environment. These interactions have been previously used to coat wild–type viruses with various materials, such as oxides,

sulfides and metal particles [67-69]. In addition to these well-defined assembly features, the TMV can be genetically programmable and renewable in large quantities. The virus is also a robust biological platform, showing stability for pH values from 2-10 for several hours and temperatures up to 60°C without destruction of its integral shape.

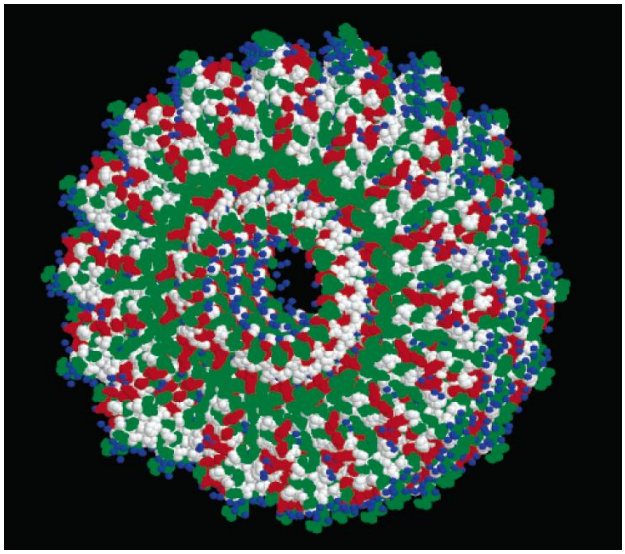

Figure 3.2: Model of the TMV disk showing the various amino acids [67].

3.2 Engineered Mutations

While the electrostatic interactions discussed in the previous section are important in associating metal precursor ions onto the wild-type virus template, the strength of this bond is rather weak and therefore limits the use of the wild-type TMV in the realization of nanostructured materials. To address this issue, engineered modifications of the virus coat proteins have been the focus of research ever since the first complementary DNA cloning of the TMV was demonstrated by Dawson *et al* in 1986 [64]. Two of the first mutations were produced to investigate the amino acid interactions. These were point mutations of the glutamic acid to glutamine and of the

aspartic acid to asparagine, resulting in the mutants E50Q and D77N respectively [62]. These modifications were found to contain only 25% of RNA to protein ratio as compared to the wild-type particle and they demonstrated an elongation in the virion from 300 nm to 940 nm.

Engineered modifications have also been created to improve the functionality of the TMV as a nanoscale template by the addition of reactive functional groups to the inner and outer surface protein structure. The introduction of one or two cysteine residues in the coat protein open reading frame have been previously reported [24, 66] and were found to significantly enhance metal deposition as compared to the wild-type virus. Cysteines are amino acids that contain thiol groups, and the sulfur molecules of these thiols are hypothesized to take part in strong, covalent-like bonds with various metal ions and atoms. The strength of these bonds as well as the mild conditions needed for the interactions make the thiol group coupling an effective method for coating the TMV with biological and inorganic materials.

In this work, we use the TMV1cys, an engineered mutant of the wild-type virus containing one cysteine residue in each of its coat proteins. This modification is achieved through a process known as *PCR-based site-directed mutagenesis*, which has been extensively described elsewhere [64]. A complementary DNA clone is produced from the wild-type RNA and then used for the introduction of the cysteine. The specific codon (TGT in the case of cysteines) is introduced in the third position of the coat protein open reading frame. Following this process, RNA transcripts of this modified clone are used to infect the host plant, *Nicotiana tabacum* cv *Xanthi*, which acts as the factory for mass production of the virus. The infected leaves are

harvested 20 days post inoculation and the virus is purified using a typical purification process [70, 71]. Briefly, the plant leaves are frozen and then mixed in a blender with sodium phosphate buffer at the appropriate pH and chloroform, which is used to remove all unwanted cellular debris. Finally, the virus solution is extracted after the virus pellets undergo several centrifugation steps.

A schematic representation of the virus coat protein arrangement with the introduced cysteine residue is shown in Figure 3.3. Figure 3.3(a) shows a top view of the virion with the cysteines around the outer surface, while Figure 3.3(b) is an edge view showing the exposed functional groups on the 3' end.

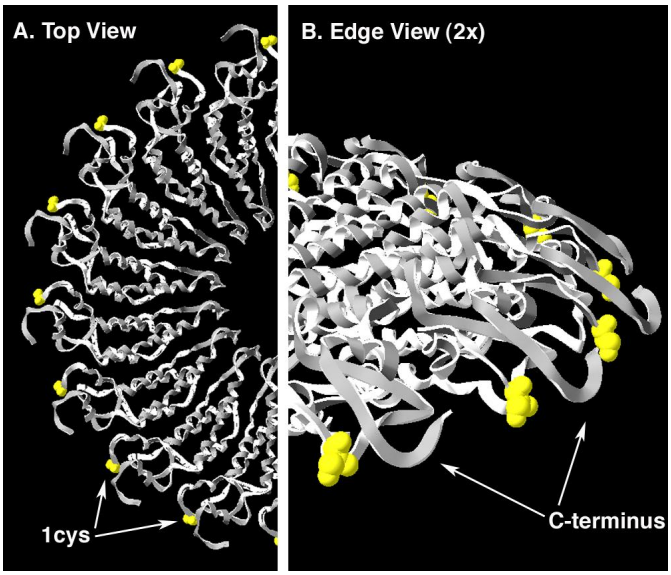

Figure 3.3: Structural location of the TMV1cys mutation: (a) Top view showing half of a coat protein layer within the TMV rod and (b) 2X magnification of an edge view for the same coat protein layer (location of the 1cys mutations are highlighted in yellow).

3.3 Metallization and Applications

The Tobacco *mosaic virus* has been used as a structural nanomaterial both in its wild-type and mutated form. Knez *et al* reported the fabrication of nickel and cobalt TMV nanowires using electroless metal deposition [68]. The authors used the

functionality of the protein chemical groups to act as linkers for metal ions as previously discussed in this chapter. The TMV virions were first activated with palladium and platinum catalysts in the presence of the appropriate reducing agents and a second electroless plating step was used to coat the virus surface with the nickel and cobalt particles, resulting in wires 3 nm wide. In addition to this electroless plating approach, Knez *et al* have also presented coating of the TMV with metal oxide nanoparticles (titanium oxide and aluminum oxide) using a gas-phase atomic layer deposition process [67].

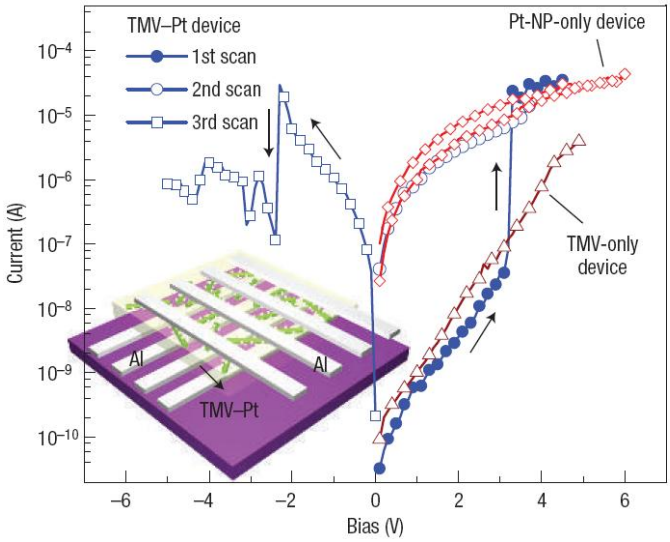

Figure 3.4: Concept and operation of the TMV-based digital memory device of [74].

A very interesting application of metal-coated wild-type viruses was presented by Tseng et al in [72], where an electronic device was fabricated from these biomolecules coated with platinum nanoparticles (NP). The device demonstrated a digital memory behavior based on conductance switching between the ON and OFF states. Figure 3.4 shows the concept of this device, which consists of dispersed TMV-Pt nanowires in an insulating polyvinyl alcohol (PVA) matrix, sandwiched between

two aluminum electrodes. The graph in Figure 3.4 shows an abrupt increase by three orders of magnitude in the measured current as the voltage is scanned above 3.1 V. The authors attribute this conductance switching effect to charge transfer from the RNA to the platinum nanoparticles under the high electric field, which in turns changes the conductivity of the material system.

Modified versions of the virus have also been used in the development of nanoscale templated materials. Lee *et al* deposited gold, silver and palladium clusters on the surface of the TMV2cys mutation using electroless deposition, and these reactions resulted in more dense coatings compared to the unmodified viral template [66]. Yi *et al* demonstrated the assembly of the TMV1cys mutation onto microfabricated electrodes through the use of a DNA hybridization process [73]. The viral particles were tagged with a DNA molecule and a fluorescent marker and assembled onto a chitosan-mediated gold substrate to bind with the complementary chain, as shown in Figure 3.5.

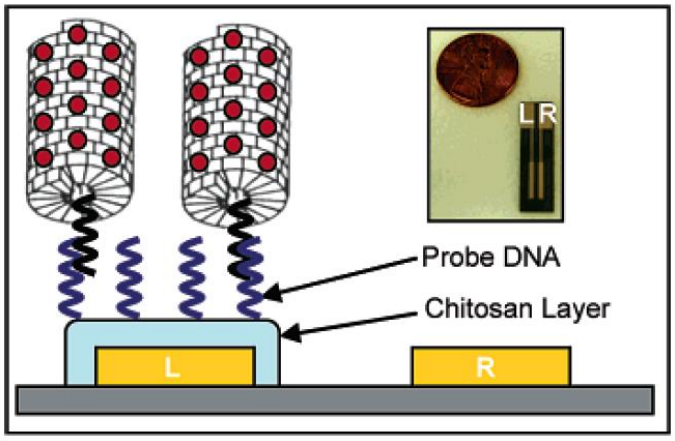

Figure 3.5: Demonstration of the patterned TMV assembly on a chitosan-mediated electrode using DNA hybridization [73].

As discussed in Chapter 1, Royston *et al* [24] has used the TMV1cys as a template for the fabrication of high-surface area nickel and cobalt electrodes, demonstrating the positive effect of the introduced cysteine residue in achieving dense and conformal metallic coatings. In addition to demonstrating their application as battery electrodes, the authors estimated the increase in surface area introduced by the virus-structured materials. Briefly, SEM images with a 1 μm^2 area were taken for virus concentrations of 0.01, 0.1 and 1 mg/mL. A particle count was performed in these images and the surface area was calculated by assuming an average coating thickness of 30 nm and particle length of 700 nm. These two assumptions were based on TEM cross-sections of TMV coated gold substrates, as shown in Figure 3.6. The increase in surface area was estimated to be 6±2 for the 0.01 mg/mL concentration and 13±3 for the 0.1 and 1 mg/mL concentrations.

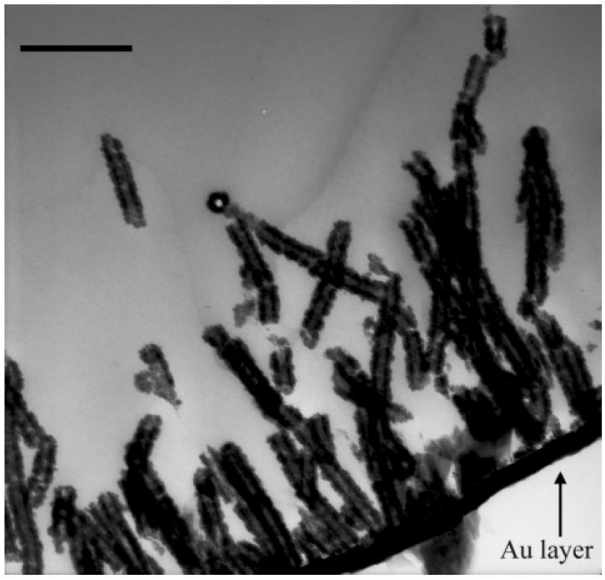

Figure 3.6: TEM image showing a 70 nm thick cross-section of nickel-coated TMV1cys attached perpendicular to a gold surface. Scale bar is equal to 300 nm [24].

Chapter 4: Design and Fabrication

The device design and fabrication development are presented in this chapter. After a short introduction of the selected battery system, the design concept is discussed. Following this, process flow is presented and the three key fabrication processes used in this work are described in detail. These include the TMV self-assembly and metallization, the structural SU-8 fabrication, and the bonding procedure with the intermediate SU-8 layer.

4.1 Design

4.1.1 Chemistry

The microbattery developed in this study uses a nickel-zinc chemistry with a potassium hydroxide (KOH) aqueous electrolyte. This is a secondary alkaline battery that does not require any special separators for proper operation and it can be constructed using standard MEMS fabrication processes. Its rechargeable nature allows it to be used in applications where many charge-discharge cycles are necessary, such as part of a larger hybrid power supply or a wireless sensor network.

Royston *et al* performed XPS elemental analysis of the nickel coated TMV surface to investigate the composition of the nanostructured electrode [59]. Metallic nickel, nickel oxide (NiO) and nickel hydroxide ($Ni(OH)_2$) were detected, suggesting the following two reactions are occurring during battery operation:

$$2NiOOH + Zn \leftrightarrow 2Ni(OH)_2 + Zn(OH)_2 \qquad (1)$$

$$NiO + Zn \leftrightarrow Ni + ZnO \qquad (2)$$

The right direction of the arrow corresponds to the discharge portion of the cycle while the left direction represents the charge reaction. During charging, nickel hydroxide and metallic nickel are converted into nickel oxyhydroxide and nickel oxide, respectively. When the direction of the current is reversed and the battery is discharged, the zinc electrode is oxidized and the electrons are transferred from the external circuit to reduce the cathode active materials back to their previous state. The expected theoretical voltages for these two chemistries are 1.73 V and 1.5 V respectively, based on the standard electrode potentials of the active components, as discussed in Chapter 2.

4.1.2 Device

The microbattery device is comprised of two electrodes separated by an electrolyte cavity defined in SU-8. A three-dimensional view of the battery showing the different layers is illustrated in Figure 4.1. The bottom electrode (cathode) consists of nickel coated TMV nanostructures assembled on a gold current collector and the top electrode (anode) is a zinc plate machined with macroscale techniques. The two layers are bonded through an intermediate thin SU-8 layer. Electrolyte is introduced via through-holes machined in the zinc (500 μm in diameter, see Appendix B). The electrochemical cell active areas are 0.36 cm^2, 0.64 cm^2 and 1 cm^2 as defined by lithography and the overall device footprint is 2 cm x 2 cm to ensure a strong bond with the anode and facilitate testing of the various geometries. The separation

between the electrodes is determined by the two SU-8 layers. The structural SU-8 layer was fabricated with thicknesses of 55 μm and 100 μm while the bonding layer was found to add to this spacing by approximately 10 μm.

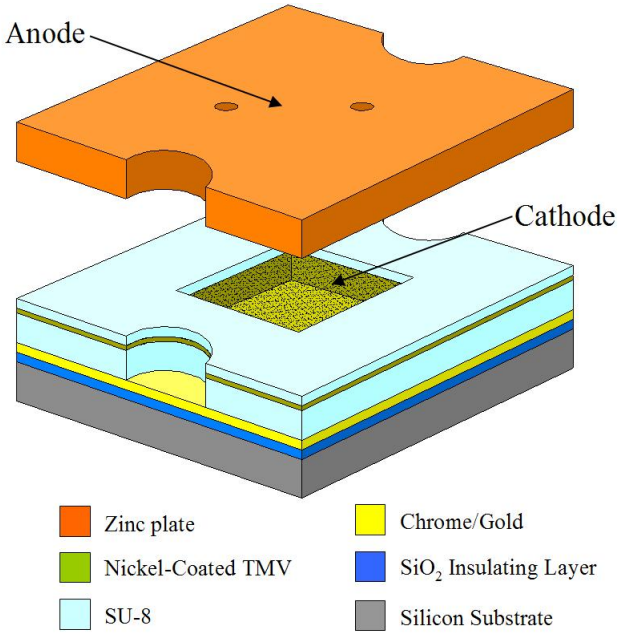

Figure 4.1: Three-dimensional view of the microbattery layers.

4.2 Fabrication

4.2.1 Process Flow

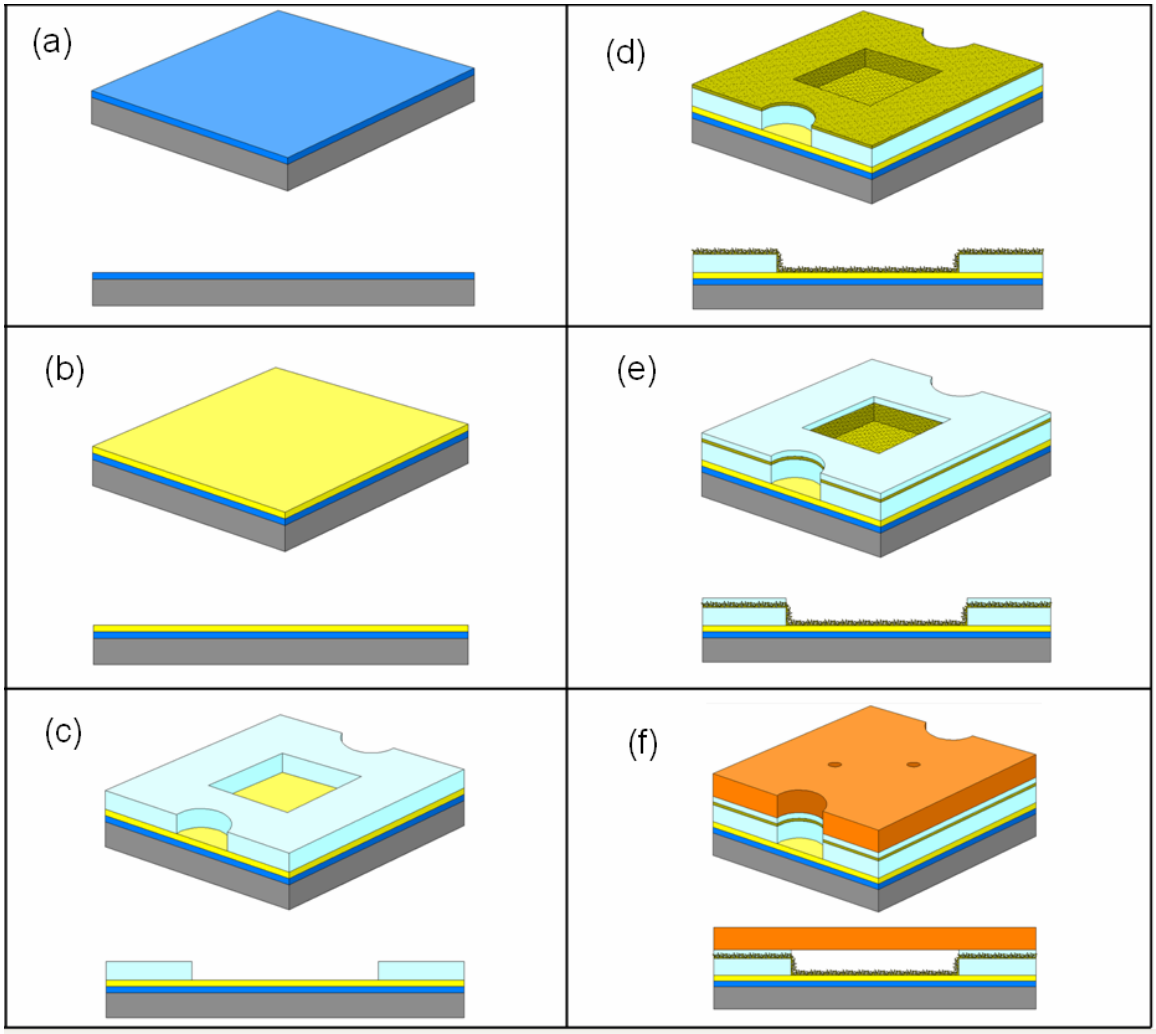

Figure 4.2: Fabrication process flow: (a) LPCVD of a SiO2 film, (b) E-beam evaporation of Cr/Au, (c)structural SU-8 lithography, (d) TMV self-assembly and coating process, (e) patterning of the bonding SU-8 layer, and (f) bonding with the zinc anode.

The fabrication process flow for the microbattery is shown in Figure 4.2. The process begins with the deposition of a 0.5 μm silicon dioxide (SiO_2) film on a 4 inch silicon wafer (fig. 4.2(a)) using a low-pressure chemical vapor deposition (LPCVD) technique (this step was performed by the clean-room stuff at the Maryland Nanocenter facilities). This dielectric layer is used to isolate the substrate from the

cathode as well as to protect the substrate from etching in the potassium hydroxide electrolyte. Chrome and gold layers are then e-beam evaporated on the dielectric to thicknesses of 20 nm and 250 nm respectively (fig. 4.2(b)), using a CHA evaporator at the Laboratory for Physical Sciences clean-room and a standard metal deposition recipe. Chrome is used as an adhesion layer, while gold serves as the cathode current collector and the base for the TMV assembly. Following this, the structural SU-8 layer is patterned on the wafer (fig. 4.2(c)). After SU-8 lithography, the wafers are covered with a thin photoresist layer (Shipley 1813, spun at 3000 rpm for 30 seconds) and diced using a wafer dicing saw to individual cathode layers. At this point, the fabrication continues at the die level with the TMV self-assembly and nickel coating (fig. 4.3(d)). Since TMV was found to adhere to SU-8 as well, a stamp-and-stick process with an intermediate thin SU-8 film was developed to facilitate bonding with the zinc anode (fig. 4.2(e) 4.2(f)).

The following sections present the three developed processes in this work, which include the structural SU-8 fabrication, the TMV self-assembly and coating process, and the adhesive bonding using the intermediate SU-8 film.

4.2.2 Structural SU-8

As shown in the design section, the device walls, electrolyte cavity, and cathode electrical connections are defined using one photolithography step with SU-8. A transparency mask was designed in L-Edit and it is shown in Figure 4.3. This mask contains a total of 12 devices per wafer (4 inch) with 3 different footprint areas, and alignment marks to facilitate dicing without the use of an additional mask for the

metal layer. Since SU-8 is a negative-tone photoresist, the polarity of this mask is inverted so that transparent and opaque areas are interchanged during printing.

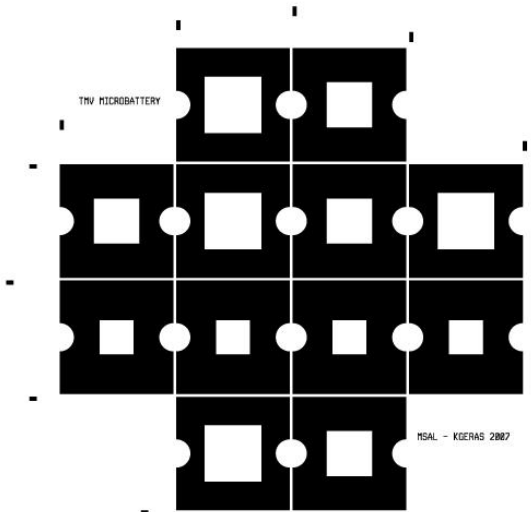

Figure 4.3: Image of the transparency mask used for the structural SU-8 fabrication

Due to the large area of the structures and the existence of sharp, concave corners, stress control and adhesion had to be precisely controlled. This is important to avoid crack formation and peeling respectively during development. In addition to these inherent concerns with SU-8 lithography, little information was available in the open literature for fabrication of large structures on a gold substrate; therefore an application-specific process had to be developed. As a starting point for the fabrication process development, the suggested recipe for SU-8 50 processing from the manufacturer was used on a test silicon wafer. Briefly, the photoresist was dispersed using a pipette with a large orifice to avoid bubble formation and then spun using two ramping steps at the desired thickness. After spinning, the edge bead was removed manually using a cue tip. The wafer was soft-baked first at 65°C and then at 95°C for the suggested times, exposed and then post-exposure baked similarly before it was finally developed.

A limitation in using this recipe was imposed by the available equipment. More specifically, the mask aligner (Quintel Q4000 contact aligner) did not have an optical filter at 365 nm to block irradiation at lower wavelengths, for which SU-8 shows significant absorption. The use of a broadband lamp required an overexposure compared to the doses suggested in the manufacturer data sheet to avoid crack formation that was initially observed. Figure s 4.4(a) and (b) show two optical images of the SU-8 structures after development without and with overexposure respectively.

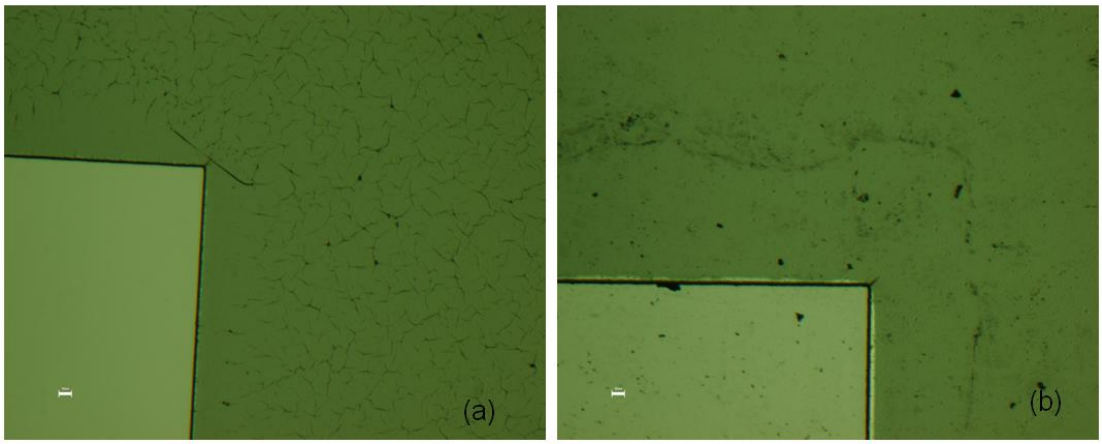

Figure 4.4: (a) Crack formation for underexposed structures and (b) resolved problem after exposure.

Direct application of the developed recipe on a gold substrate required better temperature control, due to poor adhesion of the SU-8 on this surface, as suggested by studies reported elsewhere [74, 75]. To reduce thermal stresses, the soft-bake step was performed using a 5°C/min ramp from 65°C to 95°C. Crack formation and peeling off the structures were observed when an identical process was used on a gold-covered wafer. Several solutions were examined to address this issue; the exposure dose was increased by approximately 75% to compensate for back-reflections from the gold surface and all the baking steps were ramped from room

temperature to 95°C, where the wafers remained for prolonged periods. These slight modifications did not repeatably improve the adhesion problems in all the areas of the wafer.

Two more drastic solutions were then investigated in parallel. The first approach involved the use of a thin SU-8 layer as an adhesion promoter, while the second approach was based on decreasing the baking temperatures and increasing the baking and cool-down times as suggested in [76], to induce lower thermal stress on the SU-8 structures and assist proper polymerization of the film.

Processing using the thin SU-8 layer relied on creating a film of similar structure on which adhesion of the battery walls is expected to be superior as compared to the gold surface. SU-8 2002 was spun to a thickness of 3 μm and patterned using the transparency mask of Figure 4.5. After development, structural SU-8 lithography was done on the patterned wafer with the same mask, using slow ramps for both baking steps from room temperature to 65°C and from 65°C to 95°C. While adhesion of the structures was found to be significantly improved, misalignment of the two steps using one mask only could not be avoided (Figure 4.5(a)), posing a limitation in the use of this process for the final device.

The effect of reducing the baking temperatures was investigated by applying the previously developed process with minor modifications. Before lithography, the wafers were thoroughly cleaned in acetone, methanol and isopropyl alcohol, rinsed in water, and then dehydrated for 15 minutes at 200°C to make sure the surface of the gold is clean, a parameter necessary to ensure better adhesion. The temperature was ramped from 25°C to 75°C, and the wafers remained at this temperature for almost

twice the time as before for both the soft-bake and post-exposure bake steps. Similarly, the wafers were cooled down to room temperature for more than two hours before processing steps. This time may be excessively long, it ensures however reproducible cooling for all experiments. As shown in Figure 4.5(b), no cracks or peeling off of the structures were observed. The adhesion was examined briefly by an attempt to delaminate the film using a piece of scotch tape. Mechanical stability of the SU-8 layer under this quick test, which imposes forces far greater than those expected during operation of the device, suggests that adhesion is indeed approved with this modification due to the lower residual stress. Table 4.1 summarizes the processing parameters for the two structural SU-8 layers developed in this work.

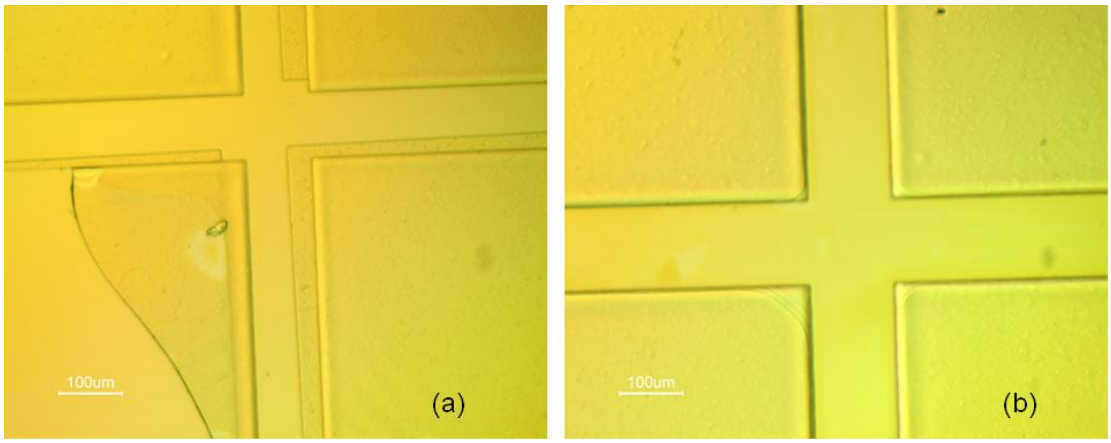

Figure 4.5: SU-8 structures using (a) SU-8 2002 as adhesion promoter and (b) reduced baking temperatures

TABLE 4.1 – PROCESS PARAMETERS FOR STRUCTURAL SU-8 LAYER.

Step	**55 µm thickness**	**100 µm thickness**
Spread cycle	600 rpm, 100 rpm/s, 10 s	600 rpm, 100 rpm/s, 10 s
Spin cycle	2500 rpm, 270 rpm/s, 30 s	1100 rpm, 200 rpm/s, 27 s
Soft-bake	75°C at 5°C/min, total of 40 mins	75°C at 5°C/min, total of 2hrs and 15 mins
Exposure	360 mJ/cm^2	800 mJ/cm^2
Post-exposure bake	75°C at 5°C/min, total of 35 mins	75°C at 5°C/min, total of 1 hr and 15 mins
Development	5 mins with agitation	8 mins with agitation

4.2.3 TMV Self-assembly and Metallization

The TMV1cys self-assembly and nickel metallization are solution based reactions that take place at room temperature. The process, which has been developed by Royston using the technique of catalyst activation and electroless deposition presented by Knez *et al* [68,69], is completed in three steps. These include binding of the virus onto a gold surface through the surface exposed thiols of the cysteines (step 1), activation of the TMV surface with palladium to catalyze the electroless plating reaction (step 2), and finally coating of the virus with nickel (step 3) [68-69]. The electroless formation of palladium clusters and nickel active material use ionic metal baths mixed with the appropriate reducing agent. Detailed information regarding all solution preparation is given in Appendix A. A schematic of the process is shown in Figure 4.6.

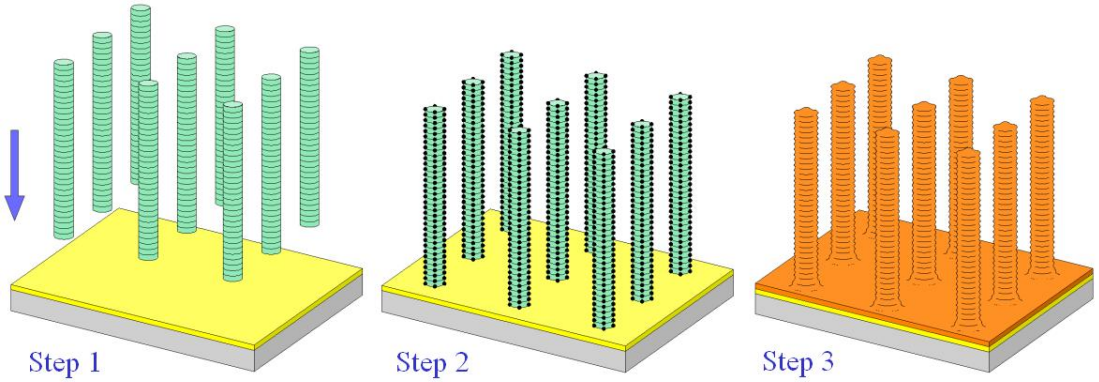

Figure 4.6: Schematic representation of the TMV assembly and nickel coating process: the TMV binds on the gold surface (step 1), activated with a palladium catalyst (step 2) and finally coated with nickel (step 3).

The gold surface is cleaned in a 1:1 mixture of acetone and ethanol in an ultrasonic bath for 15 minutes and then rinsed thoroughly with de-ionized water. This step is important to make sure that the substrate is free of any organic contaminants

that can severely deteriorate the virus attachment. After drying with nitrogen, the chip is immersed in a solution containing TMV1cys at a concentration of 0.3 mg/mL in a 0.1 M sodium phosphate buffer at pH 7 and allowed to incubate overnight in a magnifier box (2'' x 2''). The overnight reaction is done to maximize attachment of the nanostructures onto the substrate. During this stage, the viruses self-assemble onto the gold through the exposed cysteines at the 3' end. It is hypothesized that the favorable attachment of the TMV is perpendicular to the substrate, because the cysteines of the outer surface are recessed within the pits and grooves of the virus structure, as was schematically illustrated in Figure 3.3. Therefore, these functional groups are not directly exposed to gold. In practice, mechanisms such as head to tail alignment of virions, existence of broken TMV rods and random distribution within the solution result in divergence from an absolute vertical alignment.

Following the TMV assembly on the substrate, the surface exposed cysteine residues are activated with a palladium catalyst through reduction of Pd^{2+} to Pd^{0} in the presence of a hypophosphite reducing agent. Palladium is used as a catalyst for the nickel plating process as suggested in previous work [68,69]. More specifically, a 10 mM sodium tetrachloropalladate (Na_2PdCl_4) solution is mixed with a 0.1 M phosphate buffer in 1:15 ratio and the reaction on the virus surface proceeds during a second overnight step in the dark, as the solution is light-sensitive. The 1:15 mixing ratio of buffer to palladium salt has been experimentally found to be an optimum threshold for completion of the successive coating reaction. Proper activation was verified for higher ratios at the expense of excessive use of materials.

The final step of the coating process uses a standard electroless nickel plating solution at pH 7 containing 0.1 M nickel chloride ($NiCl_2$), 0.15 M sodium tetraborate ($Na_2B_4O_7$), and 0.25 M glycine in the presence of 0.5 M dimethylamine borane ($(CH_3)_2NHBH_3$)) as the reductant [68,69]. The plating bath is mixed with DI water in a 1:1 ratio and the gold surface is immersed in the mixture for two to four minutes. This duration is directly affected by the ratio of buffer to catalyst used in the activation step, with faster depositions observed for higher ratios. The overall deposition reaction is shown below:

$$3Ni^{2+} + (CH_3)_2NHBH_3 + 3H_2O \rightarrow 3Ni + B(OH)_3 + (CH_3)_2NH_2^+ + 5H^+$$

At this point, nickel metal is directly reduced onto the palladium catalyzed sites. Since hydrogen gas is a by-product of the reaction, this step is performed in an unsealed container. Due to the autocatalytic nature of the nickel reaction, this electroless plating process results in a continuous nickel coating around the virus surface on the order of 20-40 nm [24], suggesting a notable improvement in the coating density compared to similar attempts with the wild-type TMV.

Using this process, cathode layers with and without viral nanostructures were fabricated. The procedure for the planar nickel electrodes was identical, with the exception of the first step that was not performed to correspond to a zero concentration of virus. Figure 4.7 shows SEM images of nickel electrodes with and without TMV coatings. As anticipated, the alignment of the virus for this concentration is not completely vertical; however the increase in surface area is evident. The verticality and packing density of the viral structures were found to be

dependent on the TMV concentration as shown in Figure 4.8. Thorough investigation of this effect will be the focus of future research work.

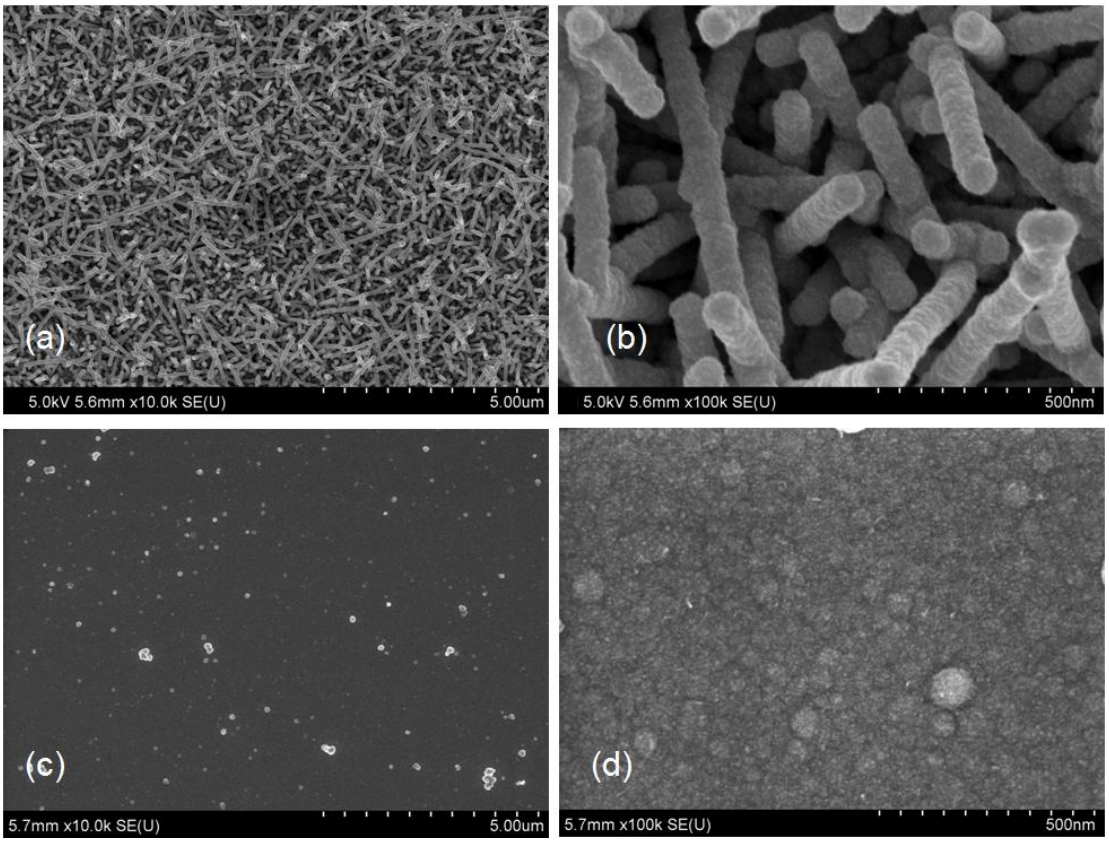

Figure 4.7: SEM images at two magnifications of nickel electrodes with (a,b) and without (c,d) TMV coatings.

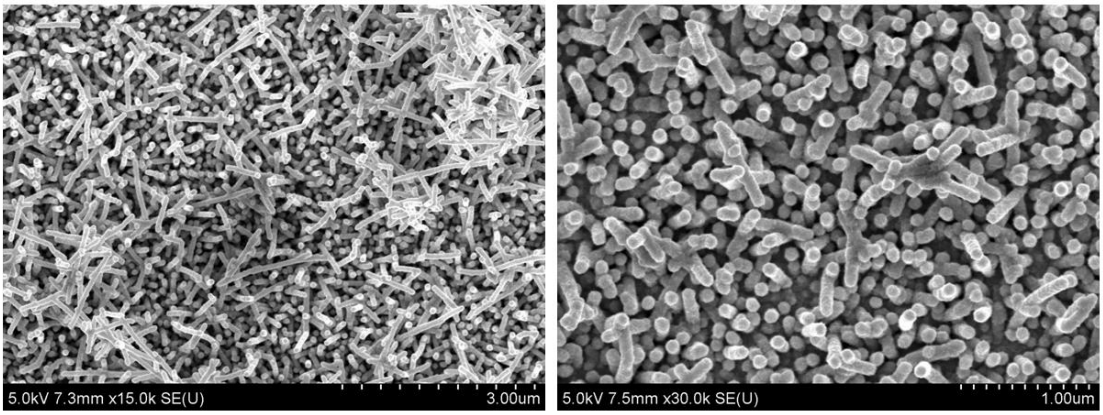

Figure 4.8: SEM image of nickel electrodes at TMV concentrations of 0.05 mg/mL (left) and 0.01 mg/mL(right).

4.2.4 Adhesive Bonding with SU-8

The need for the development of a special process for the bonding of the anode and cathode layers emerged from experiments that showed very good attachment of the TMV structures onto SU-8. This is believed to occur due to interactions of the hydrophobic amino acids of the virus with the hydrophobic polymer. This experimental observation suggests that a short-circuit between the two layer would occur unless all of the structural SU-8 area that is in contact with the zinc is electrically isolated.

This limitation was addressed by the development of a die-by-die "stamp-and-stick" process using an intermediate thin SU-8 layer. The thin SU-8 film acts as an adhesive for the low-temperature bond required between the metal and the polymer while at the same time it electrically isolates the two electrodes. A thin SU-8 5 layer is spun at a final speed of 1600 rpm on a dummy silicon wafer. A spread cycle at 600 rpm with a ramp of 100 rpm/sec is used and the final spin speed is also ramped at 200 rpm/sec. Directly after spinning, the die are pressed against the wafer transferring a thin viscous SU-8 layer to the structural SU-8 film. The zinc anode, which is thoroughly cleaned with solvents and DI water prior to assembly, is then manually aligned with the cathode and the bonded layers are baked on a hotplate at 100°C with a ramp of 5°C/min for 5-10 minutes with a small weight applied on top to strengthen the bond. The dummy silicon wafer which served as the carrier for the adhesive layer is rinsed in acetone, methanol and IPA and it can be re-used multiple times without imposing any limitations in the bonding procedure.

Figure 4.9(a) shows an SEM image of the bonded device, while Figure 4.9(b) is an image of the TMV structures on the lithographically patterned SU-8 covered by the intermediate layer (without the zinc plate). After cooling down, the bond is inspected manually, showing robustness under moderate forces applied to detach the two surfaces. Detaching of the zinc anode from the silicon die was observed only after excessive force was applied with a pair of tweezers inserted between the layers. Electrical isolation was verified by resistivity measurements performed with a digital multi-meter, showing values that in most cases exceeded the resolution of the instrument and in worst cases were in the range of 2-8 MΩ.

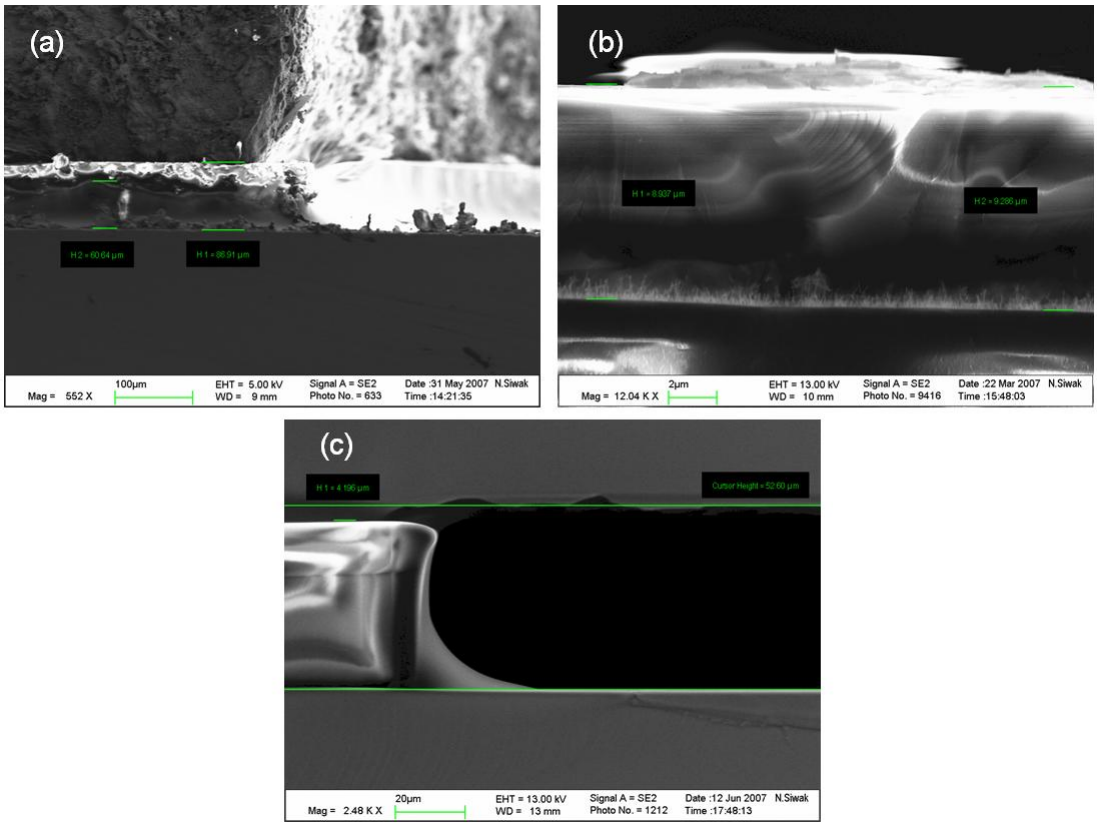

Figure 4.9: SEM images of (a) a zinc piece bonded with the patterned SU-8 layer, (b) TMV structures on the structural SU-8 layer covered in SU-8 and (c) a bonded test structure of two silicon chips used in estimating the bond thickness.

To investigate the additional thickness introduced by the bonding layer, several cathode layers were fabricated at a thickness of ~50 μm, bonded with silicon chips of identical dimensions using the developed process, and the bond thickness was evaluated by measuring the distance between the two layers with SEM and subtracting the structural layer thickness. An example of such an assembly is shown in Figure 4.8(c). The bonding layer for 12 test structures was found to fluctuate between 5 μm and 16 μm with an average value of approximately 10 μm. This average is assumed to be the additional-to-lithography spacing in all successive microbattery characterization experiments. The unpolished side of a silicon wafer was used as a means of evaluating the bond interface because the assembled stack could be easily cleaved for inspection. On the other hand, dicing of the final device through the thick zinc plate could not be achieved without a catastrophic impact on the bond. Figure 4.10 shows an image of an assembled device diced in half and its cross-sectional schematic.

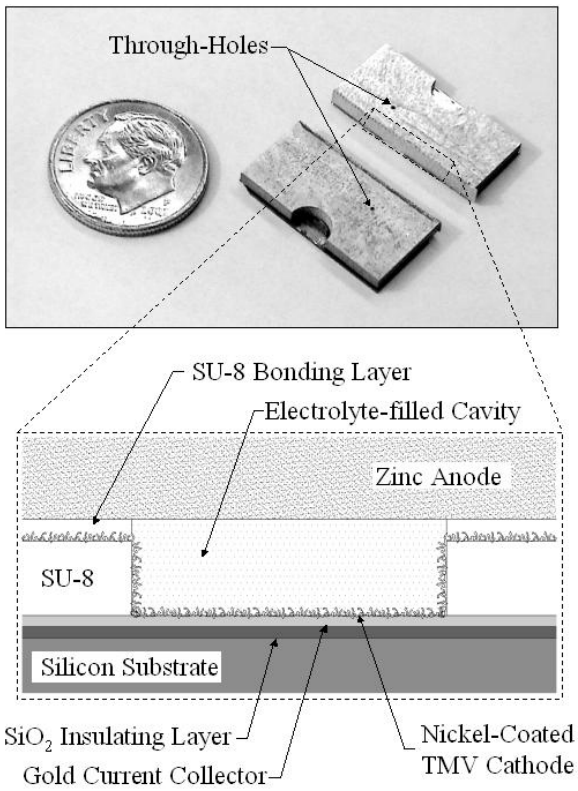

Figure 4.10: Image of a microbattery diced in half and its cross-sectional schematic.

Chapter 5: Testing and Results

This chapter presents the testing apparatus prepared and used for the electrochemical characterization of the fabricated microbatteries and discusses in detail the results of the experiments. The development of a novel microfluidic package for battery testing is reported and the operation of a potentiostat, an instrument commonly used in electrochemical analysis and employed in this study, is explained. The results section focuses on demonstrating proper charge-discharge behavior of the TMV microbatteries under different operating conditions as well as quantitatively exhibiting the benefits of using high surface area nanostructured materials for battery electrodes. Finally, the effects of design parameters are analyzed through capacity measurements for two different electrode spacings.

5.1 Testing Apparatus

This section describes the two individual components that facilitated testing of the electrochemical cells, the microfluidic package and interface as well as the potentiostat operation.

5.1.1. Microfluidic Package

A novel packaging scheme that allows testing of various device geometries was developed and is shown in Figure 5.1. The package is made of LEXAN, a Plexiglass-like rigid plastic material, and consists of two plastic manifolds that are

held together with bolts. The bottom component serves as a base for the microbatteries while the top piece contains multiple fluidic ports drilled through the plastic in an elbow structure. Fluidic interface is made through stainless steel tubing and Teflon tubulation (TFLN-063, TUBN-063, Scanivalve Corp. WA, USA) which has been glued with epoxy on the sides to facilitate electrolyte circulation. The microbattery is placed on a rubber film at the base of the package for mechanical stability and electrical isolation.

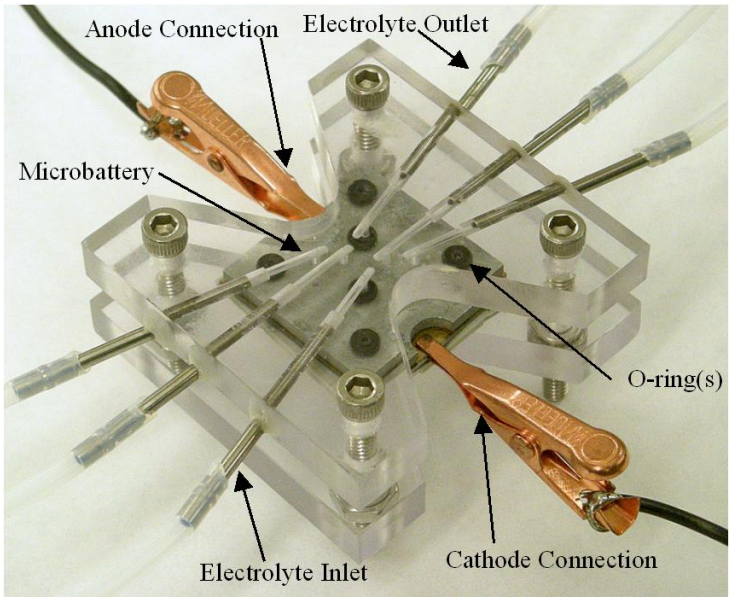

Figure 5.1: Image of a packaged microbattery showing the fluidic and electrical connections

Mounting of the microbattery device on the package is performed in two steps: first, two rubber o-rings are aligned with the holes machined in the zinc and four additional o-rings are placed in each corner for mechanical support. The top package component is then placed on top of the device through alignment of the fluidic ports with the o-rings and holes. Finally, the assembly is flipped upside down, the bottom package component is aligned on top using the outer holes machined in the plastic and bolts are inserted and tightened to keep the two pieces in place. The

electrolyte is introduced manually using a syringe and electrical connections with the battery terminals are made with alligator clips as shown in Figure 5.1. The AutoCAD design files are illustrated in Appendix B along with the corresponding dimensions.

5.1.2 Potentiostat Operation

The devices are tested using a potentiostat (Solartron, model 1287 A, Hamphsire, UK) and commercial software for electrochemical analysis (Corrware, Solartron, Hampshire, UK). A potentiostat charges and discharges the battery at a constant current density within pre-determined voltage or time limits. During the charge cycle, current is provided to the device through the electrical connections for a pre-set time or until the upper voltage limit is reached. When either of these two conditions is met, the discharge begins. During this process, current is drawn from the battery terminals until a lower voltage limit is reached or until the discharge exceeds the time set by the operator. The capacity is calculated by the product of the discharge time and the current and it represents the total charge generated in the reaction, as discussed in Chapter 2. An image of the potentiostat software interface where all these specifications are set is illustrated in Figure 5.2.

The parameters used for the electrochemical characterization of the microfabricated devices are summarized in Table 5.1, where the second column corresponds to the first round of experiments and the second column shows the modified parameters based on the findings and reports of the initial testing [77, 78]. It should be noted that, during this initial round, the devices were charged and discharged at constant current rates, which corresponded to constant current densities

different for each footprint geometry. This specification was changed in the second round of experiments and these devices were cycled under constant current density conditions, by adjusting the current for each geometry. In both cases, the charging current is set higher than the discharge value as suggested in [60], to make up for any lost capacity in the nickel electrode during discharge.

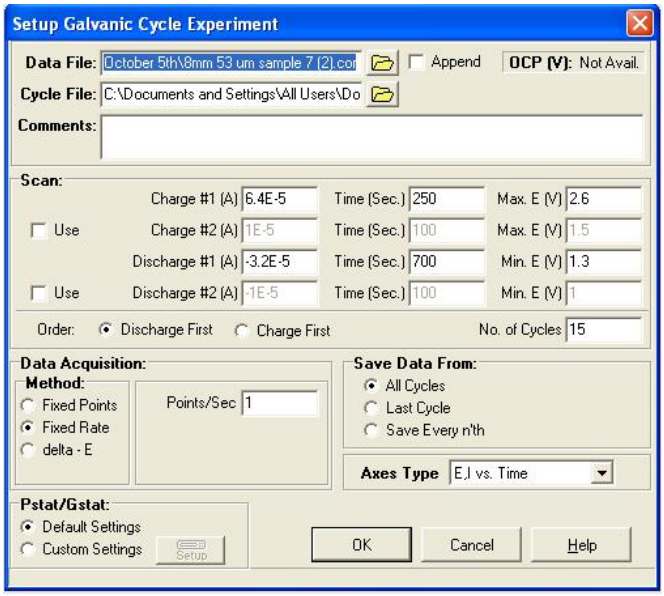

Figure 5.2: Image of the potentiostat software interface

TABLE 5.1 – POTENTIOSTAT PARAMETERS

Specification	**1st round of testing**	**2nd round of testing**
Programmed operation	15 cycles	15 cycles
Upper voltage limit	3 V	2.5 V
Lower voltage limit	0.5 V	1.3 V
Charge cycle	1 mA	100 μA/cm^2
Discharge cycle	50 μA	50 μA/cm^2
Charge time limit	90 s	250 s
Discharge time limit	300 s	500 s

The electrolyte used in this study was a one molar (1 M) KOH solution. The concentration of this solution is notably lower compared to the values suggested in the open literature [42, 49, 60, 61]. It was observed that the zinc plate corrodes rapidly at higher concentrations, severely limiting testing capabilities. The selected concentration has lower ionic conductivity resulting in higher internal resistance and lower capacity. However, it allows device testing and comparison between the different configurations for more extended periods of time.

5.2 Initial Results

According to the processes described in Chapter 4, the battery electrodes are fabricated in the discharge state. In this first round of experiments, the nickel cathodes were pre-charged before full device assembly. This was achieved by immersion of the die in a beaker containing 1M KOH solution and a dummy zinc

anode. This macroscopic assembly was cycled briefly using the potentiostat and the cathode layers were then bonded with the zinc anode as described previously.

Figure 5.3 shows the charge-discharge curve of a TMV microbattery with an active area of 0.64 cm^2 and a cavity height of 100 μm for the first nine cycles of operation. The device was cycled according to the parameters of Table 5.1, where the upper and lower voltage limits were selected according to observations made during the characterization of the half-cells by Royston *et al* [59]. A high charging current for a short time period was selected to achieve faster cycling of the devices and limit the impact of zinc corrosion in KOH. The battery exhibits the appropriate cycling behavior, since during repeated cycling, more nickel is converted to nickel oxide and nickel oxyhydroxide, increasing the amount of surface area that participates in the reaction. This results in an increase in the time of discharge and consequently in microbattery capacity.

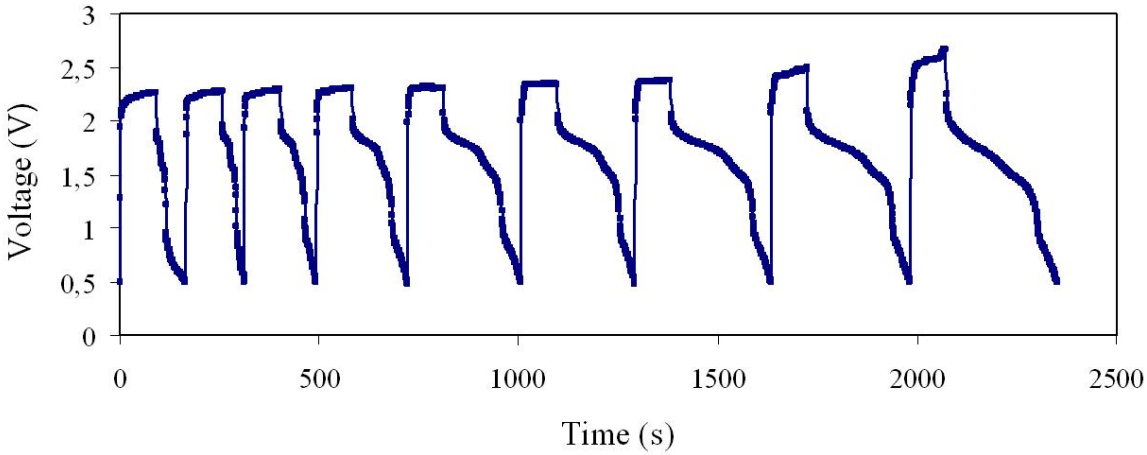

Figure 5.3: Charge-discharge curve of a TMV microbattery under the initial testing conditions.

5.3 Characterization

Based on the results of these initial characterizations, four changes have been made for the successive experiments:

1) The charge current was decreased significantly in the same order of magnitude as the discharge value. This was done because during charging, the *IR* voltage drop seemed to affect the charge voltage and caused the upper limit to be reached fast.
2) The upper and lower voltage limits were adjusted to 2.5 V and 1.3 V respectively. The first value was adjusted in accordance with the decrease in the charge current, while the second limit was reduced to the voltage for which it was experimentally observed that the battery delivers most of its useful capacity.
3) The devices were not pre-charged before full assembly. This was done to prevent effects of non-repeatability that could be observed during the pre-assembly charging for different electrodes. This would additionally allow a more accurate comparison between devices with and without viral nanostructures.
4) The devices were cycled under constant current densities, to allow testing under identical conditions for different footprint geometries.

The characterization of the microfabricated batteries in the following sub-sections will focus on verifying proper device operation for the new parameters, investigating the effect of TMV coating on battery capacity by comparing with

unmodified devices, studying the repeatability of the batteries and finally investigating the effect of electrode gap on battery capacity.

5.3.1 Charge – Discharge Response

The charge discharge curve of a TMV microbattery with an active area of 0.64cm^2 and a spacing of 65 μm is shown in Figure 5.4. This device has been cycled according to the modified parameters and its capacity is calculated within the range of 2 V to 1.3 V. The graph shows the first eight cycles of operation where the capacity increases gradually from 1.22 μAh/cm^2 to 3.38 μAh/cm^2, similarly to Figure 5.3. In addition to showing the appropriate behavior as explained before, the device charge-discharge profile is smoother and quite similar to theoretically expected curves which were shown in Figure 2.4. It is also observed that the voltage during the charge part of the cycle is much lower compared to the values of Figure 5.3, demonstrating the effect of decreased charging current density.

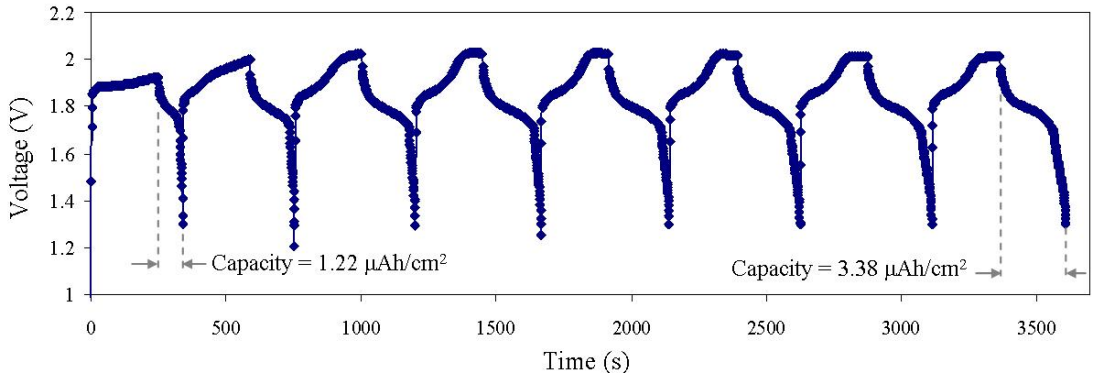

Figure 5.4: Charge-discharge curve of a TMV microbattery under modified operating conditions for the first 8 cycles of operation.

This particular device operated successfully for 30 cycles reaching a maximum capacity of 4.45 μAh/cm^2, which is the maximum capacity value reported for the nanostructured microbatteries when characterized under these conditions. The capacity versus cycle number for this device is plotted in Figure 5.5. Capacity values up to approximately 8 μAh/cm^2 were calculated when the cathode layers were pre-charged, which indicates the potential of the nanostructured nickel electrode to reach much higher values in future designs.

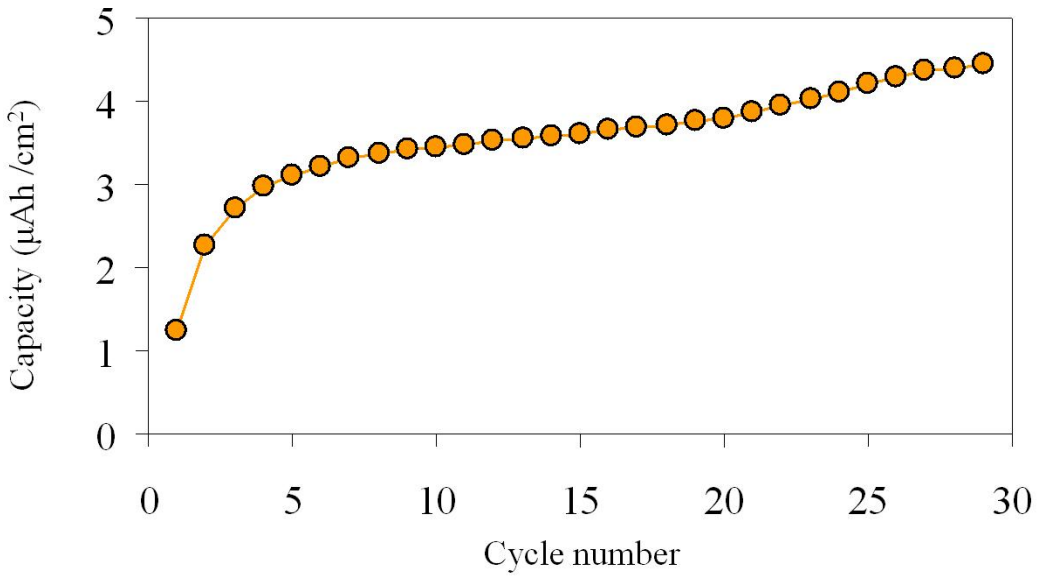

Figure 5.5: Capacity versus cycle number for a TMV modified device with 0.64 cm^2 footprint area and electrode spacing of 65 μm.

5.3.2 Effect of TMV Coating

Devices with and without viral nanostructures were compared to investigate the effect of increased surface area. Figure 5.6 shows the first discharge for three TMV modified and three unmodified devices with electrode gaps of 65 μm. The average value of the discharge capacity for the nanostructured microbatteries is increased by a factor of six compared to the average capacity of those with planar nickel electrodes. In Figure 5.6 it is also observed that the operating voltage of the

microbatteries remains mostly in the range of 1.7 V. According to the discussion in section 2.2, this implies that more of the nickel hydroxide material is present on the surface of the cathode. This is caused by the temperature induced effects during baking of the assembled devices.

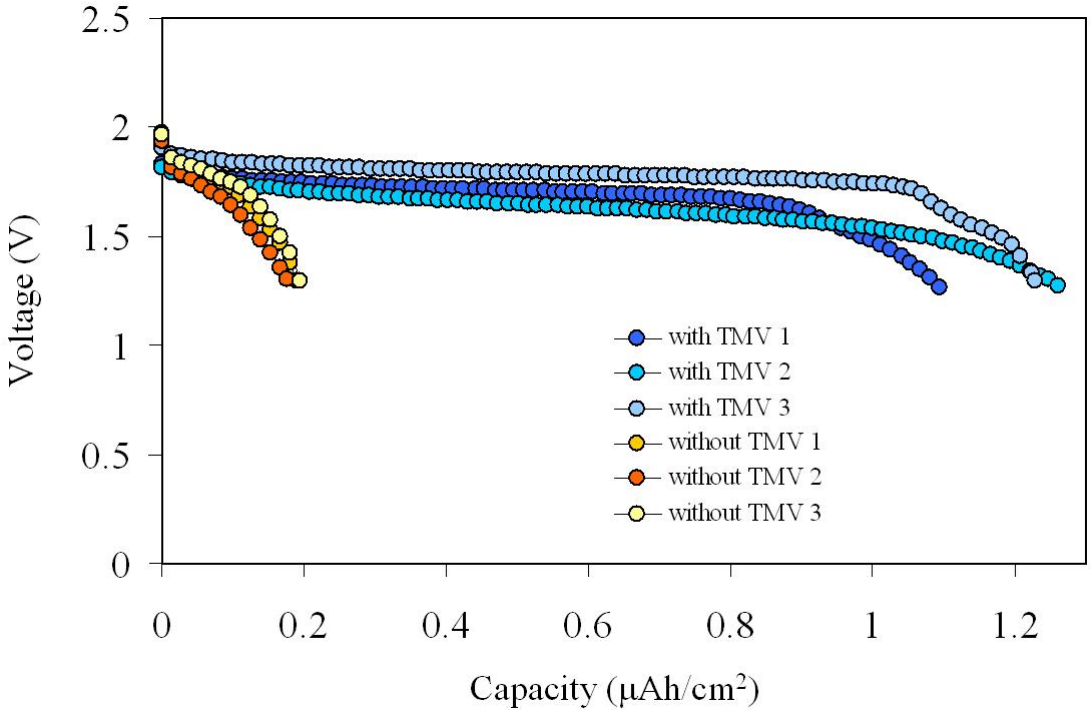

Figure 5.6: Initial discharges of cells with and without TMV coatings.

Testing of several identical nanostructured devices demonstrated that, while battery capacity is similar during the first cycle, discrepancies can be observed thereafter.

5.3.3 Device Repeatability

In some of the devices tested the upper voltage limit of the potentiostat was reached, the cycling behavior became increasingly erratic and the capacity degraded abruptly. This behavior is primarily attributed to variability in the as-fabricated devices, such as the surface quality of the zinc plate, the thickness of the nickel

coating, improper sealing introduced during bonding and short-circuiting between the zinc anode and the nickel coated sidewalls of the SU-8 cavity due to dendrite formation. Figure 5.7 is a representative example of the capacity versus cycle number for three such devices with identical footprint areas and electrode spacings.

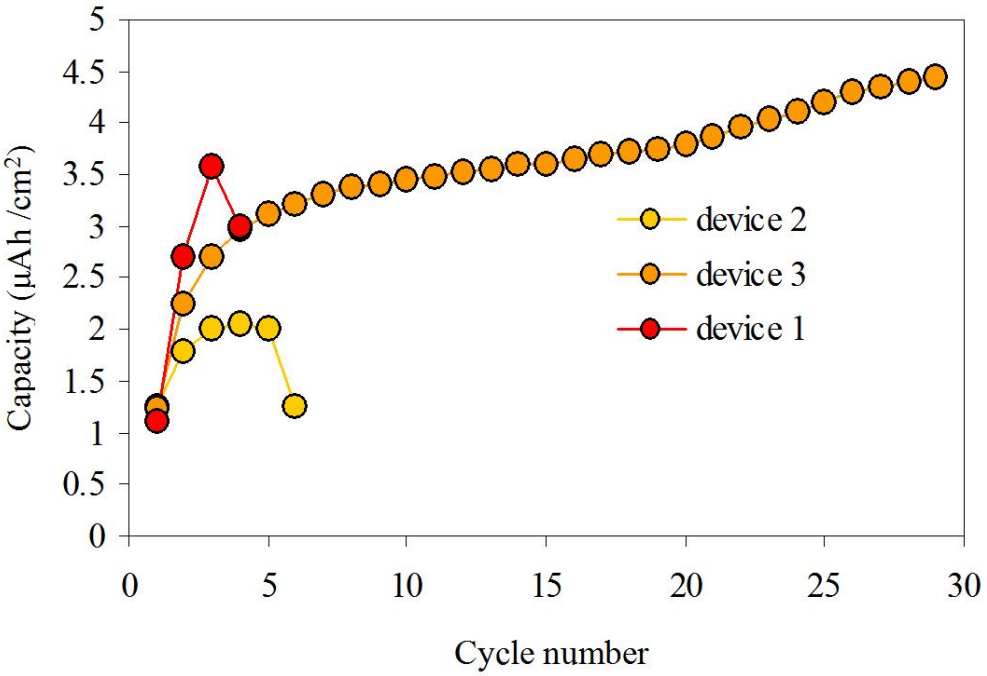

Figure 5.7: Capacity versus cycle number for three TMV modified devices with 0.64 cm^2 footprint area and electrode spacing of 65 µm.

This lack of repeatability explains why only the first discharges are compared as a more accurate indication of the effect of increased surface area. It should also be noted that, while the unmodified devices exhibited smooth cycling operations, the maximum capacity was observed during the first cycle in most of the examined cases and it was found to slowly degrade for the successive cycles. The cycling was stopped manually before lifetime exhaustion of the devices, since comparison was intended only for the first cycle. If maximum capacities were to be compared, the effect of TMV coating would correspond to an increase in capacity by a factor of up to 20.

5.3.4 Effect of Electrode Gap

Devices with different cavity heights were tested to investigate the effect of electrode spacing. Intuitively, it is anticipated that the decreased gap between the anode and cathode will cause a decrease in the internal resistance within the electrolyte and this will affect the operating voltage of the cell, which will now be higher. This is illustrated in the graph of Figure 5.8, which shows one discharge cycle for devices with spacings of 65 μm and 110 μm respectively.

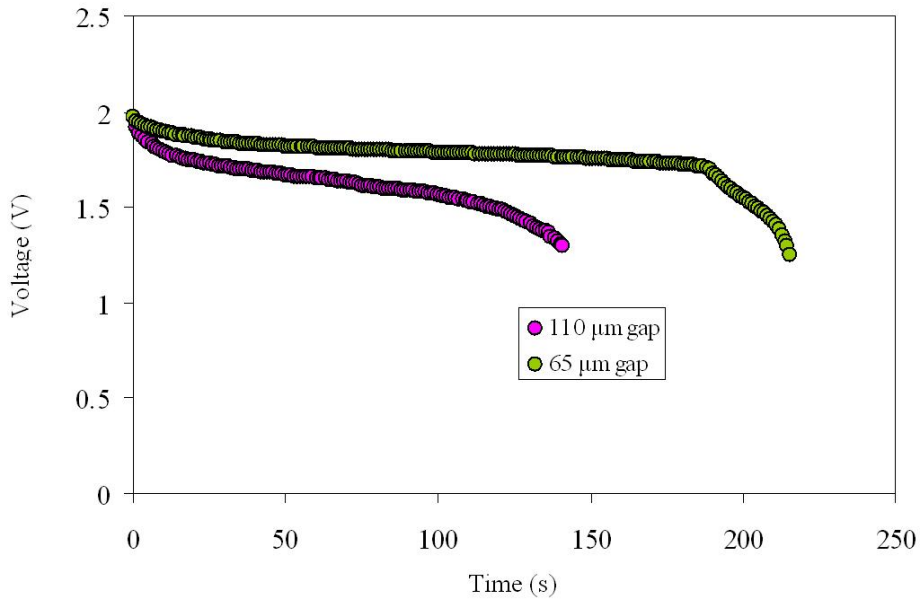

Figure 5.8: Voltage versus time graph for one discharge cycle of devices with different electrode gaps.

Figure 5.9 shows the capacity versus cycle number for electrode spacings of 65 μm and 110 μm. The capacity is calculated in the operating range of voltages for the microbattery, as defined from all previous experiments. It is observed that a decrease in electrode spacing by roughly a factor of two results in an approximately equivalent increase in capacity in the range of 2 V to 1.3 V (the lower limit of operation). This suggests that the resistance within the electrolyte is the dominant

factor that defines the battery capacity and future work should focus on decreasing the ion diffusion distances between the electrodes.

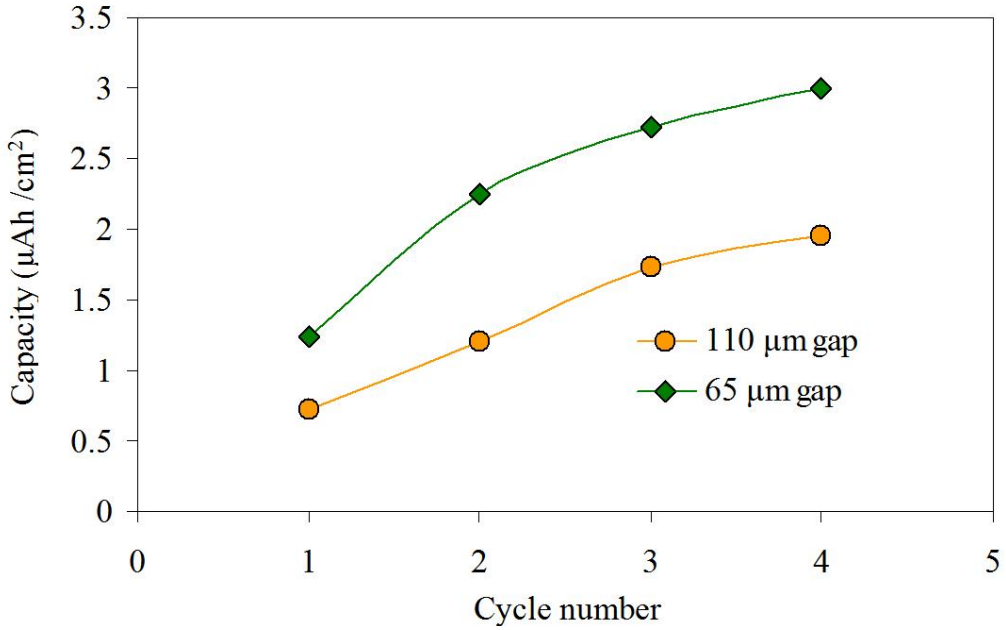

Figure 5.9: Capacity versus cycle number for devices with different electrode spacings.

5.4 Summary

The experimental characterization results presented in this section demonstrate the feasibility and usefulness of high surface area nanostructured electrodes in the development of MEMS fabricated batteries. The virus-structured devices exhibited the expected appropriate cycling behavior, with the capacity increasing after each cycle as a result of more cathode material activation. The capacity increased until the point where the upper voltage limit of the potentiostat was reached, indicating the onset of erratic behavior and performance degradation. This onset appeared at different cycle numbers for various devices, ranging from four up to thirty cycles of operation. The maximum capacity observed for devices with

viral electrodes was 4.45 μAh/cm^2 when these cells were tested from the discharged state, while values up to 8 μAh/cm^2 were calculated for microbatteries that were pre-charged before device assembly. The effect of TMV coating in battery performance was demonstrated through a six-fold increase in capacity during the initial discharge compared to device with planar electroless nickel cathodes. This comparison is considered to be most value for the first cycle of operation, because similar behavior was repeatably observed for this time-frame. If the maximum capacities are taken into consideration, this factor raises up to twenty. Finally, the effect of electrode spacing was quantified through testing of devices with different separation between the electrodes. It was found experimentally that a decrease in the gap by roughly a factor of two causes an approximately equivalent increase in microbattery capacity in the working voltage range of interest.

Chapter 6: Future Work and Conclusions

This chapter presents the limitations of the current work and discusses solutions to address these issues. Some preliminary results towards this direction are reported and an outlook to future designs is presented. Finally, the Thesis is concluded with a brief summary of the research activities, experimental results and impact of this work.

6.1 Continued Work

6.1.1 Limitations

While the scope of this research work was not to develop a high-performance MEMS battery but to demonstrate the feasibility of using the *Tobacco mosaic virus* for nanostructured MEMS battery electrodes, several factors limited the quantitative performance of the first prototype devices. Common problems encountered in nickel-zinc batteries involve zinc corrosion in the alkaline electrolyte and uneven redistribution of chemical byproducts on the anode, leading to dendrite formation [60, 79]. Rapid zinc degradation was observed in many of the devices tested for this work, preventing cells from reaching maximum capacity. Examination of the electrode surfaces after testing showed formation of a substantial passivation layer on the zinc anode, which causes an increase in cell resistance during charge. In these cases, the upper voltage limit of the potentiostat was reached before the devices were fully charged and the capacity of the battery dropped rapidly. This is attributed to the lower

available surface area of the zinc electrode, as compared to the nanostructured nickel cathode.

Variability in the fabrication process is believed to be another significant factor contributing to inconsistencies in device operation. As discussed in Chapter 5, some key issues related with the fabrication process involve the surface quality of the zinc anodes, which are machined from a plate of the metal and could vary significantly from device to device, and imperfections during bonding. For example, it was observed in some cases that during alignment of the two layers the viscous SU-8 would pour inside the electrolyte cavity, reducing the active area. Another factor that is believed to affect the operation lifetime of the fabricated batteries is the close proximity of the SU-8 sidewalls to the zinc anode. As was discussed in Chapter 4, TMV adheres well to SU-8 and possible formation of dendrites around the edges (which can be up to several microns as reported previously [79]) is a likely cause of short-circuiting (Figure 6.1) and performance degradation that was often observed after some cycles of operation.

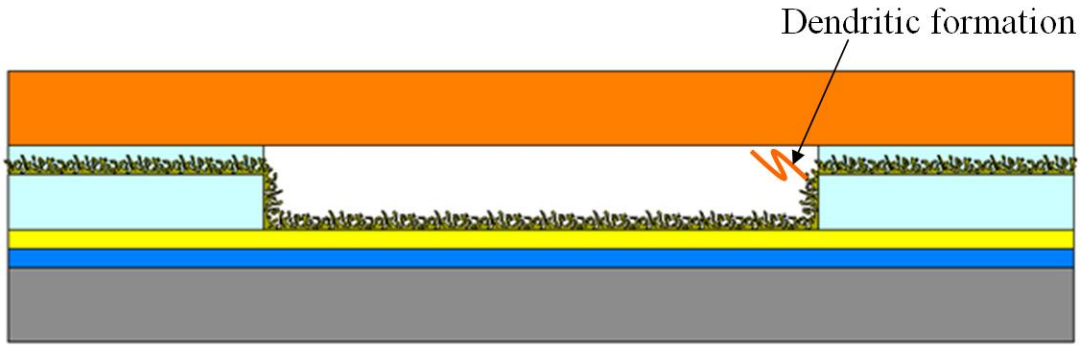

Figure 6.1: Schematic representation of a likely mechanism for device failure – dendrite formation from the zinc anode to the conductive SU-8 sidewalls.

To address these limitations, future work will focus on improving the anode and the fabrication process. The benefit of the TMV coatings can be fully realized by

incorporating high aspect ratio nanostructures on the zinc electrode as well. The development of such a high surface area and high conductivity anode will result in increased capacity while reducing the effects of passivation. Moreover, TMV processing at the wafer level and alternative packaging methods are expected to increase the yield of the devices. The following sections show some preliminary results towards this direction and discuss some possible future designs and applications that could benefit from the TMV biofabrication approach.

6.1.2 Nano- and micro-fabrication development using the TMV

A key process towards the development of a batch fabrication approach is the ability to pattern the TMV selectively on specific areas of the wafer. To investigate the feasibility of such processes, photolithographic patterning of the nanostructures was explored through the lift-off technique and post-processing was examined through compatibility with over steps that have been used in the developed fabrication process.

In this experiment, a gold-covered silicon chip was used as the substrate. The die was masked in half of its area using adhesive tape and then a positive Shipley 1813 photoresist was spun at 3000 rpm for 30 seconds to define a 1.6 μm thick layer. After spinning, the masking tape was removed from the substrate and the chip, now partially covered in photoresist, was baked on a hotplate at 100°C for 1 minute. Following soft-bake, viral self-assembly and nickel metallization were performed using the three-day process described in Chapter 4. After the electroless nickel plating step, which resulted in complete coverage over the whole silicon area, the chip was

rinsed in acetone. This step caused the photoresist to dissolve and lift off the viral nanostructures that have attached on the surface. The lithographically patterned chip was cleaned in methanol and isopropyl alcohol successively, and then examined under microscope using SEM. An image of the boundary surface between the masked and unmasked areas is shown in Figure 6.2. It is evident from this picture that the process resulted in successful removal of the TMV from the selected areas.

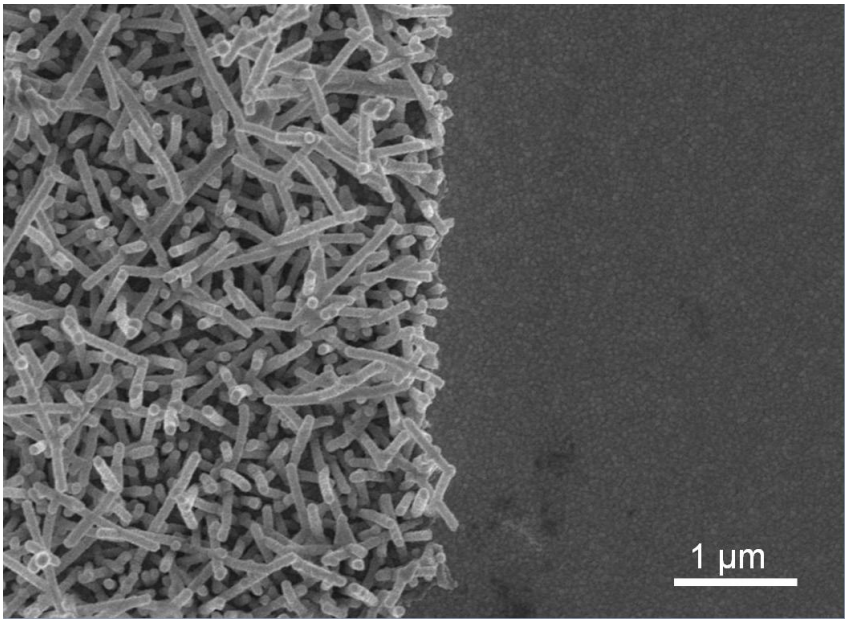

Figure 6.2: SEM image of gold-covered silicon chip with nickel-coated TMV nanostructures that have been patterned using lift-off.

The robustness of this process was further investigated through repeated imaging of the surface after pro-longed exposure of the chip in solvents as well as chemical developers. The photolithographically patterned chip was also used as the substrate for SU-8 lithography. A thick SU-8 layer was spun to a thickness of 100 µm using the process shown in Table 4.1, and then soft-baked accordingly. After this step, it was immersed in SU-8 developer to completely remove the polymer film. Examination of the nanostructured surface after this process showed no alteration in

the viruses, revealing the compatibility of this novel biofabrication technique with traditional MEMS fabrication steps.

6.1.3 Future Designs

Metallization of the TMV with different materials is another critical step that is expected to result in a significant improvement in the extracted power from the microbatteries. Since zinc electroless plating solutions are not available, approaches that are under examination include zinc electroplating or atomic layer deposition onto the nickel coated TMVs, two processes that can ensure conformal coverage of the whole viral surface. Successful development of such techniques will allow the realization of second generation designs that take advantage of the assembly properties of the TMV onto various materials. A conceptual three dimensional schematic of such a design is shown in Figure 6.3.

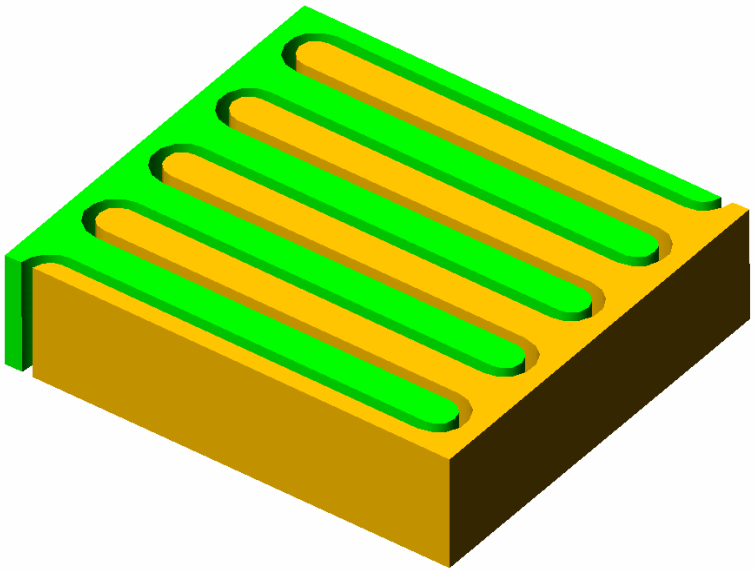

Figure 6.3: Schematic representation of a future microbattery design (the yellow and green structures correspond to two different battery electrode materials).

In this design, the unique property of TMV attachment onto SU-8 structures is utilized. The concept of operation is based on significantly increasing reactive surface area by a combination of the microfabrication and nano-scale synthesis approaches that were reviewed in Chapter 1. The interdigitated SU-8 structures provide the out-of-plane high aspect ratio structures to increase the available reactive area while maintaining device footprint, similar to the method implemented by Chamran *et al* [49]. The addition of the high aspect ratio nanostructured viruses, coated selectively through previously described processes with different battery materials, will result in a further increase in active area, altogether keeping short diffusion distances and low internal resistances. The successful development of such a design will mark a significant improvement over current approaches, as it based on fewer lithography and process steps and utilizes cost-effective techniques and less energy-intensive equipment.

In addition to their application as battery electrodes, these biological nanostructured materials can be used in other micro-power sources that require high surface area components. One such application is a micro fuel cell, which requires increased area of catalytic surface for more efficient consumption of the fuels and improved performance. The need for platinum nanocoatings has been identified by St-Pierre *et al* [80] as an important factor towards increasing the power density extracted from polymer electrolyte membrane fuel cells. The *Tobacco mosaic virus* offers a robust platform for the synthesis of this material, thereby creating new opportunities for its use in microfabricated small-scale energy conversion devices.

6.2 Thesis Conclusions

The first successful demonstration of a MEMS battery utilizing viral nanostructures was presented in this Thesis. Self-assembly and nickel coating of the Tobacco mosaic virus have been integrated into traditional MEMS fabrication processes and nickel-zinc microbatteries with nanostructured cathodes have been developed and characterized. The proof-of-concept device comprises of nickel-coated TMV particles assembled on a gold surface on a silicon wafer and a zinc anode machined with holes for electrolyte circulation. Two polymer processes in SU-8 were developed to define the separation between the electrodes, the electrical connections, as well as the bonding layer between the two different materials. The assembled TMV modified devices exhibited appropriate charge-discharge behavior for several cycles of operation, which vary from device to device. The initial capacity of these batteries was improved by a factor of six compared to cells without viral nanostructures. TMV microbatteries with smaller electrode spacings show an increase in capacity, which demonstrates the importance of electrode gap as a design parameter. These results, combined with the simplicity of the viral self-assembly and metallization process and the feasibility of full wafer-level patterning, show the potential of this technology in the development of more compact, high-performance small scale energy conversion devices.

Appendix A - Solution Preparation

Sodium tetrachloropalladate 10mM

Solution is prepared to a volume of 10 ml and aliquot in micro centrifugal tubes in volumes of 120 µl.

Use 29.419 mg of sodium tetrachloropalladate, 98%, Sigma Aldrich and mix with DI water. Store chemical away from light (not temperature sensitive).

Nickel electroless plating solution

Nickel plating solution was prepared to a volume of 25 ml and then aliquot to volumes of 0.4 ml.

Use a glass beaker and mix:

1) 0.6 g $NiCl_2$ hexahydrate (Nickel (II) chloride hexahydrate 99.9%, Sigma Aldrich)
2) 0.45 g Glycine (Glycine, tissue culture grade, Fischer Scientific)
3) 1.5 g $Na_2B_4O_7$ (sodium tetraborate, 99%, Sigma Aldrich)
4) 0.77 g DMAB (Dimethylamine borane, 97%, Sigma Aldrich). This should be added under a fume hood.

Add 25 ml DI water, this should be added last.

Place solution mixture on stir plate, covered in parafilm with a stir bar. Stir until color changes from green to blue. Periodically check pH and stop mixing when pH paper indicates the solution has reached pH 7. Store solution in the freezer.

Appendix B – AutoCAD files

Machined Zinc (Dimensions in cm)

Konstantinos Gerasopoulos
MEMS Sensors and Actuators Lab
Deptartment of Electrical and Computer Engineering
kgeras@umd.edu
301-405-1897

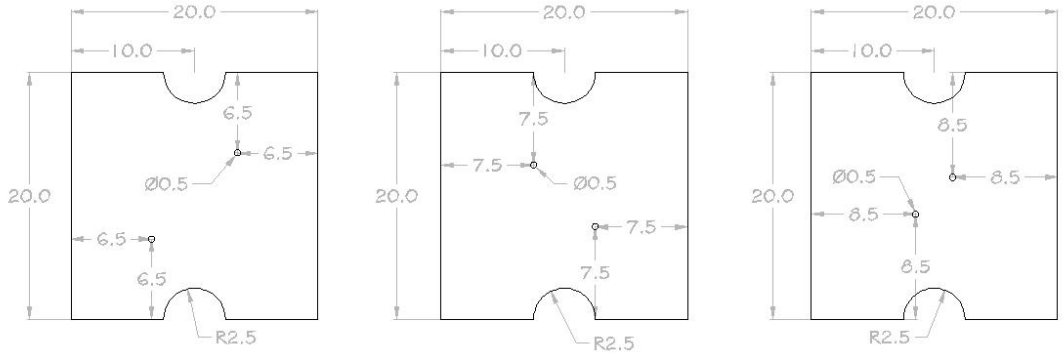

All units in milimeters - Zinc Sheet Provided

Package Designs (Dimensions in inches)

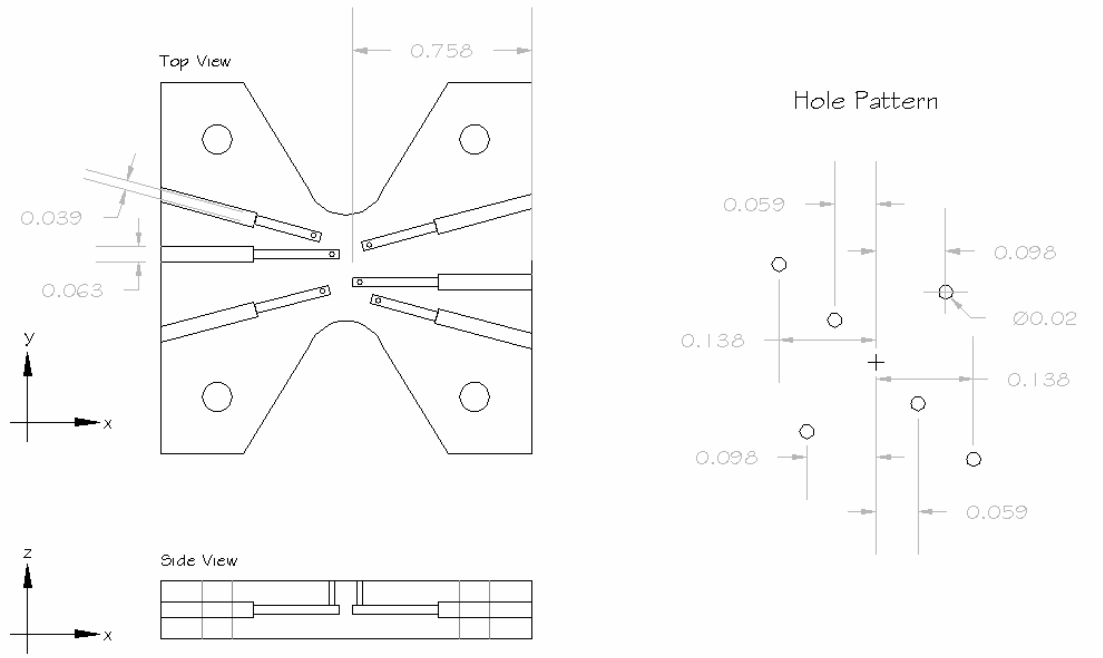

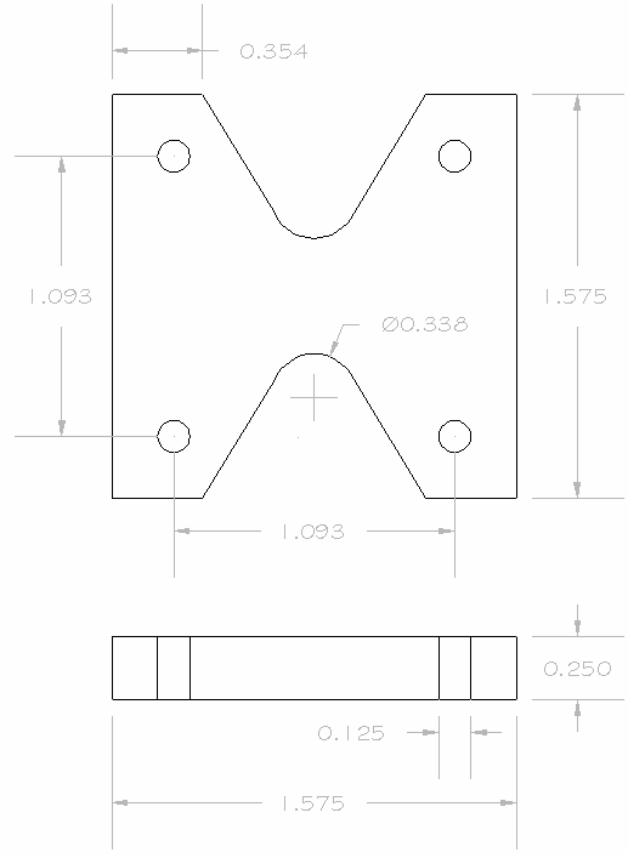
0.354
1.093
1.575
Ø0.338
1.093
0.250
0.125
1.575

References

[1] J. W. Judy, "Microelectromechanical systems (MEMS): fabrication, design, and applications", *Smart Materials and Structures*, vol. 10, 2001, pp. 1115-1134

[2] B. Warneke, M. Last, B. Liebowitz, and K. J. Pister, "Smart Dust: Communicating with a cubic millimeter computer", *Computer*, January 2001, pp. 44-51

[3] J. N. Harb, R. M. LaFollete, R. H. Selfridge, L. L. Howell, "Microbatteries for self-sustained hybrid micropower supplies", *Journal of Power Sources*, vol. 104, 2002, pp. 46-51

[4] J. W. Long, B. Dunn, D. R. C., H. S. White, "Three-dimensional battery architectures", *Chemistry Reviews*, vol. 104, 2004, pp. 4463-4492

[5] K. B. Lee and L. Lin, "Electrolyte-based on demand and disposable microbattery", *Journal of Microelectromechanical Systems*, vol. 12, no. 6, 2003, pp. 840-847

[6] A. M. Cardenas-Valencia, J. Dlutowski, J. Bumgarner, L. Langebrake and W. Morreno, "Long shelf-lie, Al-anode micro-fabricated cells activated with alkaline-H_2O_2 electrolytes", *Journal of Micromechanics and Microengineering*, vol. 16, 2006, pp. 1511-1518

[7] P. H. Humble, J. N. Harb and R. LaFollette, "Microscopic nickel-zinc batteries for use in autonomous microsystems", *Journal of the Electrochemical Society*, vol. 148 (12), 2001, pp. A1357-A1361

[8] P. Singh, S. Kaneria, V. S. Anugonda, H. M. Chen, X. Q. Wang, D. E. Reisner, and R. LaFollette, "Prototype silicon micropower supply for sensors", *IEEE Sensors Journal*, vol. 6, no. 1, 2006, pp. 211-222

[9] F. Sammoura, K. B. Lee and L. Lin, "Water-activated disposable and long shelf-life microbatteries" *Sensors and Actuators A*, vol. 111, 2004, pp. 79-86

[10] K. B. Lee, "Two-step activation of paper batteries for high power generation: design and fabrication of biofluid-and water-activated paper batteries", *Journal of Micromechanics and Microengineering*, vol. 16, 2006, pp. 2312-2317

[11] J. B. Bates, N. J. Dudney, B. Neudecker, A. Ueda, C. D. Evans, "Thin-film lithium and lithium-ion batteries", *Solid State Ionics*, vol. 135, 2000, pp. 33-45

[12] W. C. West, J. F. Whitacre, V. White and B. V. Ratnakumar, "Fabrication and testing of all solid-state microscale lithium batteries for microspacecraft applications", *Journal of Micromechanics and Microengineering*, vol. 12, 2002, pp. 58-62

[13] C. Wang, L. Taherabadi, G. Jia, M. Madou Y. Yeh and B. Dunn, "C-MEMS for the manufacture of 3D microbatteries", *Electrochemical and Solid-State Letters*, vol. 7 (11), 2004, pp. A435-438

[14] F. Chamran, Y. Yeh, H-S Min, B. Dunn, and C-J. Kim, "Fabrication of high-aspect-ratio electrode arrays for three-dimensional microbatteries", *Journal of Microelectromechanical Systems,* vol. 16, no. 4, 2007, pp. 844-852

[15] P.H. L. Notten, F. Roozeboom, R. A. H. Niessen, and L. Baggetto, "3-D integrated all-solid-state rechargeable batteries", *Advanced Materials*, vol. 19, 2007, pp. 4564-4567

[16] Y. P. Yu, E. Rahm and R. Holze, "Carbon anode materials for lithium ion batteries", *Journal of Power Sources*, vol. 114, 2003, pp. 2280236

[17] Z. Zhang, C. Dewan, S. Kothari, S. Mitra, D. Teeters, "Carbon nanotubes synthesis, characteristics, and microbattery applications", *Materials Science and Engineering B*, vol. 116, 2005, pp. 363-368

[18] R. Jiang, Y. Huang, D. Jia, L. Wang, and L. Wang, "High-capacity, high-cycling cathode material synthesized by low-temperature solid-state coordination method for lithium rechargeable batteries", *Journal of the Electrochemical Society*, vol. 154, pp. A698-A702

[19] X-J. Tang, G. Zhang, and Y-P Zhao, "Electrochemical characterization of silver nanorod electrodes prepared by oblique angle deposition", *Nanotechnology*, vol 17, 2006, pp. 4439-4444

[20] Y.H. Yuah, J. P. Tu, H. M. Wu, Y. Li and Q. D. Shi, "Size and morphology effects of ZnO anode nanomaterials for Zn/Ni secondary batteries", *Nanotechnology*, vol. 16, 2005, pp. 803-808

[21] D. E. Reisner, A. J. Salkind, P. R. Strutt, T. D. Xiao, "Nickel hydroxide and other nanophase cathode materials for rechargeable batteries", *Journal of Power Sources*, vol. 65, 1997, pp. 231-233

[22] V. L. Pushparaj, M. M. Shaijumon, A. Kumar, S. Murugesan, L. Ci, R. Vajtaj, R. J. Linhardt, O. Nalamasu, P. M. Ajayan, "Flexible energy storage devices based on nanocomposite paper", *Proceedings of the National Academy of Science (PNAS)*, vol. 104, no. 34, 2007, pp. 13574-13577

[23] K. T. Nam, D. W. Kim, J. P. Yoo, C. Y. Chiang, N. Meethong, P. T. Hammond, Y. M. Chiang, A. Belcher, "Virus-enabled synthesis and assembly of nanowires for lithium ion battery electrodes", *Science*, vol. 312, 2006, pp. 885-888

[24] E. Royston, A. Ghosh, P. Kofinas, M. T. Harris and J. N. Culver, "Self-assembly of virus-structured nanomaterials and their application as battery electrodes", *Langmuir*, vol. 24, 2007, pp. 906-912

[25] H. Lo and Y.C. Tai, "Parylene-HT-based electret rotor generator", *21st IEEE International Conference on Micro Electro Mechanical Systems (MEMS 2008), Tucson, AZ,*2008, pp. 984-987

[26] D. P. Arnold, F. Herrault, I. Zana, P. Galle, J-W Park, S. Das, J.H. Lang and M. G. Allen, "Design optimization of an 8W, microscale, axial-flux, permanent-magnet generator", *Journal of Micromechanics and Microengineering*, vol. 16, 2006, pp. S290-S296

[27] H-B. Fang, J-Q. Lu, Z-Y. Xu, L. Dong, L. Wang, D. Chen, B-C. Chai, Y. Lu, "Fabrication and performance of MEMS-based piezoelectric power generator for vibration energy harvesting", *Microelectronics Journal*, vol. 37, 2006, pp. 1280-1284

[28] Y.B. Jeon, R. Sood, J-H. Jeong, S-G. Kim, "MEMS power generator with transverse mode thin film PZT", *Sensors and Actuators A*, vol. 122, 2005, pp. 16-22

[29] W. Glatz, S. Muntwyler, C. Hierold, "Optimization and fabrication of thick flexible polymer based thermoelectric generator", *Sensors and Actuators A*, vol. 132, 2006, pp. 337-345

[30] E. Schwyter, W. Glatz, L. Durrer, C. Hierold, "Flexible micro thermoelectric generator based on electroplated $Bi_{2+x}Te_{3-x}$", DTIP of MEMS & MOEMS, 9-11 April 2008, Nice, France

[31] B. Y. Park and M. J. Madou, "Design, fabrication and initial testing of a miniature PEM fuel cell with micro-scale pyrolized carbon fluidic plates", *Journal of Power Sources*, vol. 162, 2006, pp. 369-379

[32] R. Hahn, S. Wagner, A. Schmitz, H. Reichl, "Development of a planar micro fuel cell with thin film and micro patterning technologies", *Journal of Power Sources*, vol. 131, 2004, pp. 73-78

[33] J. D. Morse, R. S. Upadhye, R. T. Graff, C. Spadaccini, H. G. Park and E. K. Hart, "A MEMS-based reformed methanol fuel cell for portable power", *Journal of Micromechanics and Microengineering*, vol. 17, 2007, pp. S237-242

[34] P-C. Su, R. Fasching and F. B. Prinz, "High surface area density nano thin film solid oxide fuel cells", *Proceedings of The Seventh International Workshop on Micro*

and Nanotechnology for Power Generation and Energy Conversion Applications (PowerMEMS 2007), Freiburg, Germany, November 28-29, 2007, pp. 19-23

[35] T. Moriuchi, K. Morishima and Y. Furukawa, "Porous carbon electrode to improve power of photosynthetic bacteria fuel cell", *Proceedings of The Seventh International Workshop on Micro and Nanotechnology for Power Generation and Energy Conversion Applications (PowerMEMS 2007), Freiburg, Germany, November 28-29,* 2007, pp. 15-18

[36] T. Kim, J. S Hwang and S. Kwon, "A MEMS methanol reformer heated by decomposition of hydrogen peroxide", *Lab on a Chip*, vol. 7, 2007, pp. 835-841

[37] T. Kim and S. Kwon, "Design, fabrication and testing of a catalytic microreactor for hydrogen production", *Journal of Micromechanics and Microenginering*, vol. 16, 2006, pp. 1760-1768

[38] W. Riedel, "Electroless Nickel Plating", *Finishing Publications Ltd, 1991*

[39] S. Furukawa and M. Mehregany, "Electroless plating of nickel on silicon for fabrication of high-aspect-ratio microstructures", *Sensors and Actuators A*, vol. 56, 1996, pp. 261-266

[40] M. Datta, S. A. Merritt and M. Dagenais, "Electroless remetallization of aluminum bond-pads on CMOS driver chip for flip-chip attachment to Vertical Cavity Surface Emitting Lasers (VCSEL's)", *IEEE Transactions on Components and Packaging Technology,* vol. 22, no. 2, 1999, pp. 299-306

[41] M. K. Md Arshad, I. Ahmad, A. Jalar, G. Omar and U. Hashim, "The effect of multiple zincation process of aluminum bond pad surface for electroless nickel immersion gold deposition", *Transactions of the ASME*, vol. 128, September 2006, pp. 246-250

[42] S. S. Bedair, B. Li, J. R. Cooper, S. Santhanam, R. D. McCullough, D. N. Lambeth and G. K. Fedder, "A CMOS MEMS gold plated electrode array for chemical vapor detection", *IEEE Sensors 2006, Korea, October 22-25*, 2006, pp. 1074-1077

[43] M. Nathan, D. Goldonitsky, V. Yufit, A. Strauss, T. Ripenbein, I. Shechtman, S. Menkin and E. Peled, "Three-dimensional thin-film li-ion microbatteries for autonomous MEMS", *Journal of Microelectromechanical Systems*, vol. 14, no. 5, 2005, pp. 879-885

[44] C. C. Tsao and E. Sachs, "Photo-electroforming: 3D geometry and materials flexibility in a MEMS fabrication process", *Journal of Microlectromechanical Systems*, vol. 8, no. 2, 1999, pp. 161-171

[45] S. Guan and B. J. Nelson, “Fabrication of hard magnetic microarrays by electroless codeposition for MEMS actuators”, *Sensors and Actuators A*, vol. 118, 2005, pp. 307-312

[46] http://www.microchem.com/products

[47] C. Wang, G. Jia, L.H. Taherabadi, and M. J. Madou, “A novel method for the fabrication of high aspect ratio C-MEMS structures”, *Journal of Microelectromechanical Systems*, vol. 14, no. 2, 2005, pp. 348-358

[48] A. Mata, A. J. Fleischman, and S. Roy, “Fabrication of multi-layer SU-8 microstructures”, *Journal of Micromechanics and Microengineering*, vol. 16, 2006, pp. 276-284

[49] D. P. Arnold, S. Das, F. Cros, I. Zana, M.G. Allen and J. H. Lang, “Magnetic induction machines integrated into bulk-micromachined silicon”, *Journal of Microelectromechanical Systems*, vol. 15, no. 2, 2006, pp. 406-414

[50] M. K. Ghantasala, J. P. Hayes, E. C. Harvey, and D. K. Sood, “Patterning, electroplating and removal of SU-8 moulds by excimer laser micromachining”, *Journal of Micromechanics and Microengineering*, vol. 11, 2001, pp. 133-139

[51] I. Song and P. K. Ajmera, “Use of a photoresist sacrificial layer with SU-8 electroplating mould in MEMS fabrication”, *Journal of Micromechanics and Microengineering*, vol. 13, 2003, pp. 816-821

[52] S. Balslev, B. Bilenberg, D. Nilsson, A. M. Jorgensen, A. Kristensen, O. Geschke, J. P. Kutter, K. B. Mogensen, and D. Snakeborg, “ Fully integrated optical systems for lab-on-a-chip applications”, *Proceedings of the 17th IEEE Conference on Micro Electro Mechanical Systems*

[53] M. A. Powers, S. T. Koev, A. Schleunitz, H. Yi, V. Hodzic, W. E. Bentley, G. F. Payne, G. W. Rubloff, and R. Ghodssi, “A fabrication platform for electrically mediated optically active biofunctionalized sites in BioMEMS", *Lab on a Chip(LOC)*, Vol. 5, 2005.pp. 583-586

[54] S. Mouaziz, G. Boero, R. S. Popovic, and J. Brugger, “Polymer-based cantilevers with integrated electrodes”, *Journal of Microelectromechanical Systems*, vol. 15, no. 4, 2006, pp. 890-895

[55] C. Friese and H. Zappe, “Deformable polymer adaptive optical mirrors”, *Journal of Microelectromechanical Systems*, vol. 17, no. 1, 2008, pp. 11-19

[56] S. Li, C. B. Freidhoff, R. M. Young and R. Ghodssi, “Fabrication of micronozzles using low temperature wafer-level bonding with SU-8”, *Journal of Micromechanics and Microengineering,* vol. 13, 2003, pp. 732-738

[57] S. Tuomikoski and S. Fransilla, "Wafer-level bonding of MEMS structures with SU-8 epoxy photoresist", *Physica Scripta*, vol. T14, 2004, pp. 223-226

[58] **B. Helbo, A. Kristensen and A. Menon, "A micro-cavity fluidic dye laser", *Journal of Micromechanics and Microengineering*, vol. 13, 2003, pp. 307-311**

[59] F. J. Blanco, **M. Agirregabiria, J. Garcia, J. Berganzo, M. Tijero, M. T. Arroyo, J. M. Ruano, I. Aramburu and K. Mayora, "Novel three-dimensional embedded SU-8 microchannels fabricated using a low temperature full wafer adhesive bonding", *Journal of Micromechanics and Micronengineering*, vol. 14, 2004, pp. 1047-1056**

[60] D. Linden, "Handbook of batteries and fuel cells", *McGraw Publishing Company, 1984*

[61] D. Linden, "Handbook of batteries", *McGraw Publishing Company, 2000*

[62] E. Royston, "Assembly of inorganic nanomaterials using *Tobacco mosaic virus*" Ph.D. Dissertation, July 2007, Purdue University

[63] A. Balandin and V. A. Fonoberov, "Vibrational modes of nano-template viruses", *Journal of Biomedical Nanotechnology*, vol. 1, 2005, pp. 90-95

[64] W. O. Dawson, D. L. Beck, D. A. Knorr, and G. L. Grantham, "cDNA cloning of the complete genome of tobacco mosaic virus and production of infectious transcripts", *Proceedings of the National Academy of Science (PNAS*), vol. 83, 1986, pp. 1832-1836

[65] D. H. Gracias, M. Boncheva, O. Omoregie, and G. M. Whitesides, "Biomimetic self-assembly of helical electrical circuits using orthogonal capillary interactions", *Applied Physics Letters*, vol. 80, no. 15, 2002, pp. 2802-2804

[66] S-Y. Lee, E. Royston, J. N. Culver and M.T. Harris, "Improved metal cluster deposition on a genetically engineered tobacco mosaic virus template", *Nanotechnology*, vol. 16, 2005, pp. S435-S441

[67] M. Knez, A. Kadri, C. Wege, U. Gosele, H. Jeske and K. Nielsch, "Atomic layer deposition on biological macromolecules: metal oxide coating of Tobacco Mosaic Virus and Ferritin", *Nano Letters*, vol. 6, no. 6, 2006, pp. 1172-1177

[68] M. Knez, A. M. Bittner, F. Boes, C. Wege, H. Jeske, E. Maiβ and K. Kern, "Biotemplate synthesis of 3-nm nickel and cobalt nanowires", *Nano Letters*, vol. 3, no. 8, 2003, pp. 1079-1082

[69] M. Knez, M. Sumser, A. M. Bittner, C. Wege, H. Jeske, S. Kooi, M. Burghard, K. Kern, "Electrochemical modification of individual nano-objects", *Journal of Electroanalytical Chemistry*, vol. 522, 2002, pp. 70-74

[70] W. L. Liu, K. Alim, A. A. Balandin, D. M. Mathews, and J. A. Dodds, "Assembly and characterization of hybrid virus-inorganic nanotubes", *Applied Physics Letters*, vol. 86, 2005, 253108

[71] G. V. Gooding and T. T. Hebert, "A simple technique for purification of tobacco mosaic virus in large quantities", *Phytopathology*, vol. 57, 1967, p. 1285

[72] R. J. Tseng, C. Tsai, L. Ma, J. Ouyang, C. S. Ozkan and Y. Yang, "Digital memory device based on tobacco mosaic virus conjugated with nanoparticles", *Nature Nanotechnology*, vol. 1, 2006, pp. 72- 77

[73] H. Yi, S. Nisar, S-Y. Lee, M. A. Powers, W. E. Bentley, G. F. Payne, R. Ghodssi, G. W. Rubloff, M. T. Harris and J. N. Culver, "Patterned assembly of genetically modified viral nanotemplates via nucleic acid hybridization", *Nano Letters*, vol. 5, no. 10, 2005, pp. 1931-1936

[74] M. Joshi, R. Pinto, V. R. Rao, S. Mukherji, "Silanization and antibody immobilization on SU-8", *Applied Surface Science*, vol. 253, no. 6, 2007, pp. 3127-3132

[75] M. Nordstrom, A. Johansson, E. S. Nogueron, B. Clausen, M. Calleja, A. Boisen, "Investigation of the bond strength between the photo-sensitive polymer SU-8 and gold", *Microelectronic Engineering*, vol. 78-79, 2005, pp. 152-157

[76] T. A. Anhoj, A. M. Jorgensen, D. A. Zauner and J. Hubner, "The effect of soft bake temperature on the polymerization of SU-8 photoresist", *Journal of Micromechanics and Microengineering,* vol. 16, 2006, pp. 1819-1824

[77] K. Gerasopoulos, M. McCarthy, E. Royston, J. N. Culver and R. Ghodssi, "Nanostructured nickel-zinc microbatteries using the Tobacco mosaic virus", *Proceedings of The Seventh International Workshop on Micro and Nanotechnology for Power Generation and Energy Conversion Applications (PowerMEMS 2007), Freiburg, Germany,* 2007, pp. 347-350

[78] K. Gerasopoulos, M. McCarthy, E. Royston, J. N. Culver and R. Ghodssi, "Microbatteries with Tobacco mosaic virus templated electrodes", *21st IEEE International Conference on Micro Electro Mechanical Systems (MEMS 2008), Tucson, AZ,* 2008, pp. 960-963

[79] F. R. McLarnon and E. J. Cairns, "The secondary alkaline zinc electrode", *Journal of the Electrochemical Society*, vol. 138, no. 2, 1991, pp. 645-664

[80] D. B. St-Pierre, M. Paquin and L. G. Freschette, “Novel electrode structure of a micro fuel cell integrating a serpentine flow field channel”, *Solid State Sensors, Actuators, and Microsystems Workshop (Hilton Head 2008), Hilton Head, SC, June 1-5*, 2008, pp. 86-87